Energy Technology
Generation, Conversion, Storage, Distribution
www.entechnol.de

Sustainable Solid Polymer Electrolytes Based on NaCMC-PVA Blends for Energy Storage Applications: Electrical and Electrochemical Insights with Application to Electric Double-Layer Capacitors

Vipin Cyriac, Ismayil, Kuldeep Mishra, Ankitha Rao, Saraswati P. Masti, and I. M. Noor*

This research proposes a novel biopolymers' blend-based solid polymer electrolyte (SPE) for electric double-layer capacitors (EDLCs). Flexible SPE films are fabricated by immobilizing sodium hexafluorophosphate ($NaPF_6$) salt in a blend of sodium carboxymethyl cellulose and poly (vinyl alcohol) using a solution-casting technique. The study employed X-ray diffraction, Fourier-transform infrared spectroscopy, scanning electron microscopy, and atomic force microscopy techniques to evaluate the structural and morphological characteristics. The electrolyte system exhibits a maximum ionic conductivity of 2.26×10^{-5} S cm^{-1} with a substantial electrochemical stability window of ≈3.56 V. Frequency-dependent electrical studies elucidate the ion dynamics of the electrolyte systems in accordance with the structural modifications within the system. The optimized electrolyte sample is employed in an EDLC device, and various performance parameters are obtained. The device demonstrates a specific capacitance of 9.53 F g^{-1}, energy density of 0.979 W kg^{-1}, and a power density of 43 Wh kg^{-1} at a current density of 0.1 mA g^{-1} and exhibited reliable performance for 3000 cycles.

1. Introduction

Polymer electrolytes are a superior choice for an electrolyte system due to their ability to meet two essential criteria that are not found in conventional liquid electrolytes and inorganic solids. First, they are leak proof and offer greater design flexibility compared to these alternatives. Second, they possess high electrical conductivity and electrochemical stability, which make them a more reliable option. Additionally, their ability to form films provides a significant advantage from a design standpoint.[1,2] Numerous methods have been implemented to improve the characteristics of polymer electrolytes, leading to the subclassification of the field into several categories, including but not limited to i) solvent-free polymer-salt complex electrolytes or solid polymer electrolytes (SPEs), ii) gel polymer electrolytes, iii) composite polymer electrolytes, and iv) ionic liquid/zwitterion-based polymer electrolytes. Thus, the scientific community has drawn to this field with great anticipation, following the groundbreaking work of Fenton et al.[3] Since then, extensive research has been carried out in this domain, resulting in the creation of various commercially available electrochemical devices, including batteries, electronic devices, pacemakers, and sensors.

V. Cyriac, Ismayil
Department of Physics
Manipal Institute of Technology
Manipal Academy of Higher Education
Manipal, Karnataka 576104, India
E-mail: ismayil.mit@manipal.edu

K. Mishra
Symbiosis Institute of Technology (SIT)
Symbiosis International (Deemed university) (SIU)
Pune, Maharashtra 412115, India

The ORCID identification number(s) for the author(s) of this article can be found under https://doi.org/10.1002/ente.202500465.

DOI: 10.1002/ente.202500465

A. Rao
Department of Electronics and Communication
Manipal Institute of Technology
Manipal Academy of Higher Education
Manipal, Karnataka 576104, India

S. P. Masti
Department of Chemistry
Karnataka University's Karnataka Science College
Dharwad, Karnataka 580001, India

I. M. Noor
Physics Division
Centre for Foundation Studies in Science of Universiti Putra Malaysia
Universiti Putra Malaysia
43400 Serdang, Selangor Darul Ehsan, Malaysia

SPE offers several benefits, but its ionic conductivity is low at room temperature.[4] Polymer electrolytes frequently exhibit a lack of mechanical strength, which can result in brittleness and a tendency to crack or tear easily.[5] In addition, certain types of polymer electrolytes can lead to corrosion and other issues by reacting with the battery electrodes. For commercial viability, polymer electrolytes must meet certain criteria, including high ionic conductivity (greater than 10^{-4} S cm^{-1}), desirable mechanical properties, and stability at electrode interfaces. These requirements are crucial for the advancement of polymer electrolytes.[6] Efforts are actively underway to address the environmental concerns associated with SPEs, which are typically derived from petroleum-based polymers that are non-biodegradable and pose environmental risks. In alignment with the 2030 agenda for sustainable development, the United Nations General Assembly established 17 Sustainable Development Goals (SDGs), including SDG 7. The objective is to guarantee access to affordable, trustworthy, eco-friendly, and modern energy sources by the year 2030. To attain this, it is necessary to devise innovative methods that utilize biomaterials instead of conventional, petroleum-based polymers.

Natural biopolymer-based films and their derivatives exhibit hygroscopic behavior and demonstrate limited mechanical strength. Enhancing these properties involves blending two or more biopolymers and incorporating specific quantities of nanofiller. Among these techniques, polymer blending has been extensively adopted owing to its straightforward sample preparation process. Additionally, it provides numerous complexation sites that facilitate salt dissolution, thereby enhancing electrolyte conductivity and electrochemical performance.[7] Cellulose, the most abundant renewable polymer in nature, is biodegradable, biocompatible, and nontoxic. NaCMC consists of two components: hydrophilic carboxyl groups and hydrophobic polysaccharides, which impart water-soluble properties.[8] Polyvinyl alcohol (PVA) is a key component of polymer electrolytes because of its colorless nature, water solubility, biocompatibility, high hydrophilicity, and complete degradability. In addition, PVA is a semicrystalline polymer that boasts exceptional photostability under UV–visible light and impressive thermal stability. These appealing characteristics make it a strong contender for a range of applications.[9] A composite of carboxymethyl cellulose (CMC) biopolymer and PVA synthetic polymer may exhibit improved mechanical properties and enhanced chemical stability, which is desirable for electrochemical applications as an electrolyte. The blend of sodium carboxymethyl cellulose (NaCMC) and PVA offers several advantages over synthetic polymers. These blends exhibit improved thermal stability, mechanical strength, and flexibility compared to individual components.[10] These blends demonstrate enhanced water absorbency, biodegradability, and biocompatibility, making them suitable for diverse applications including wound healing, drug delivery, and agriculture.[11] Additionally, researchers have explored the use of NaCMC/PVA as a polymer matrix for electrolyte systems involving protons, lithium, and sodium, which are utilized in diverse energy storage applications.[12–18] Room temperature ionic conductivity is a critical measure of an electrolyte's ability to transport ions, which directly impacts the performance of electrolytes in battery and EDLC applications. SPEs made of NaCMC/PVA typically have room temperature ionic conductivities between 10^{-6} and 10^{-3} S cm^{-1}.

The inclusion of $NaPF_6$ in polymer electrolytes effectively enhances ion migration and direct-current (DC) conductivity, rendering them suitable for various device applications. For instance, solid-state polymer electrolytes based on PEO-$NaPF_6$ exhibit promising characteristics for solid-state sodium batteries, including high ionic conductivity, large Na^+ transference number, adequate thermal stability, and long-term cycling performance.[19] Gel-polymer electrolytes based on polyacrylonitrile and $NaPF_6$ demonstrated high room-temperature ionic conductivities and could sustain over 700 charge–discharge cycles in sodium-ion cells.[20] The salt $NaPF_6$ has gained widespread recognition as a promising option for sodium-ion batteries that rely on liquid organic electrolytes. This is due to its outstanding comprehensive properties, including high solubility in organic solvents, high anodic electrochemical stability, and noncorrosive properties in the high-potential region, without utilizing Al.[19]

Hence, based on our previous work,[16–18] this study comprehensively investigates the impact of $NaPF_6$ doping on the microstructure of the NaCMC-PVA blend and ionic transport using various analytical methods, including Nyquist plot, AC conductivity, dielectric, and modulus analyses. The research also employs scaling techniques, based on the time-temperature superposition principle, to determine whether the ion conduction mechanism follows a consistent pattern at high temperatures. Lastly, the most conductive electrolyte was incorporated into an EDLC, and its performance was evaluated to assess its potential for energy storage applications.

2. Experimental Section

2.1. Chemicals used

NaCMC (185,000 g mol^{-1}, purity = 96%) and PVA (85,000 g mol^{-1}, degree of hydrolysis 86%, purity = 96%), procured from SD Fine Pvt Limited, were used to prepare the polymer blend without further purification. Sodium hexafluorophosphate ($NaPF_6$, = 167.95 g mol^{-1}, purity = 98%), from Sigma Aldrich, was the dopant. Activated carbon (AC, Kuraray, surface area = 1602 m^2 g^{-1}, purity = 99.99%), carbon black (CB), polyvinylidene fluoride (PVdF, Alfa Aesar), and 1-methyl-2-pyrrolidone (NMP, purity = 99.9%) (Alfa Aesar) were used to prepare the EDLC electrodes.

2.2. Electrolyte Preparation

The electrolyte in this study was formulated using a simple solution-casting method with deionized water as the solvent, as detailed in our previous reports.[16,17] NaCMC and PVA were combined at an 80:20 ratio, with the dopant added in 5 wt% increments up to 40 wt%, maintaining a total weight of 2 g. The weight percentage of the dopant (w_d(%)) was determined according to Equation (1). The rationale behind the selection of weight ratio of NaCMC and PVA is based on research by Saadiah, M. A., et al,[21] which identified this composition as

the most amorphous among the tested ratios. A higher degree of amorphousness is beneficial for ionic transport in polymer electrolytes.

$$w_d(\%) = \frac{m_d}{m_d + m_p} \times 100\% \quad (1)$$

Here m_p is the combined weight of NaCMC and PVA and m_d is the mass of salt. The sample labels and amount of each component are listed in **Table** 1. The thickness of the SPEs was carried out using a Mitutoyo digital screw gauge with a resolution of 0.001 mm and listed in Table 1.

2.3. EDLC Fabrication

To fabricate EDLC, 85 wt% AC and 15 wt% CB were mixed dry. A solution of 12.5 wt% PVdF in 15 mL NMP was added to the AC: CB mixture to form a slurry. The mixture (containing 1 mg of active material) was applied to a pair of stainless-steel electrodes, each measuring 1 cm^2, which functioned as current collectors. Subsequently, the electrodes underwent a drying process in a hot-air oven at 60 °C for a duration of 24 h. Following this, they were placed in a dessicator containing silica gel to ensure thorough desiccation. The cell configuration of the EDLC cell was configured as follows: AC electrode | high-conductivity solid electrolyte | AC electrode.

2.4. Electrolyte Characterization

2.4.1. FTIR Spectroscopy

Fourier-transform infrared (FTIR) spectroscopy was used to identify potential interactions among the constituents (polymer-polymer and polymer-salt) of the prepared samples. An FTIR spectrometer (Shimadzu, IR spirit) operating in attenuated total reflectance mode recorded the FTIR transmittance spectra at room temperature. Spectra were captured across the wavenumber range of 400–4000 cm^{-1} to analyze molecular vibrations and chemical bonds in the samples.

Table 1. Sample label and weights of the SPE components along with its thickness.

Designation	NaCMC/PVA: $NaPF_6$ [wt%:wt%]	NaCMC/PVA [g]	$NaPF_6$ [g]	Thickness [mm]
F0	100:0	2	0	0.059
F5	95:5	1.9	0.1	0.079
F10	90:10	1.8	0.2	0.113
F15	85:15	1.7	0.3	0.130
F20	80:20	1.6	0.4	0.103
F25	75:25	1.5	0.5	0.177
F30	70:30	1.4	0.6	0.164
F35	65:35	1.3	0.7	0.093
F40	60:40	1.2	0.8	0.184

2.4.2. X-Ray Diffraction

The X-ray diffraction (XRD) patterns of the SPE films were recorded in reflection mode within the 2θ range of 5° to 90°, at a scanning speed of 2° min^{-1}. Monochromatized Cu-Kα radiation ($\lambda = 1.5406$ Å) was utilized, generated by applying 40 kV and 15 mA to the X-ray tube of the Rigaku Mini Flex 600 diffractometer.

2.4.3. Electrochemical Impedance Spectroscopy

An impedance analyzer (Hioki IM3570 Impedance Analyzer, Japan) was used to record the dielectric response of the SPEs over a broad temperature range of 298–393 K and a frequency range of 50 Hz to 4.5 MHz. To prevent nonlinear effects, the applied root mean square voltage was maintained at 0.01 V during the measurements of Z' and Z''. The complex dielectric permittivity ε^* was obtained as

$$\varepsilon^* = \varepsilon'(f) - j\varepsilon''(f) = \frac{Z''}{2\pi f C_0(Z'^2 + Z''^2)} - j\frac{Z'}{2\pi f C_0(Z'^2 + Z''^2)} \quad (2)$$

The complex conductivity $\sigma^*(f)$ is given as

$$\sigma^* = \sigma'(f) - j\sigma''(f) = j2\pi f \varepsilon_0(\varepsilon' - j\varepsilon'') \quad (3)$$

where σ' is real part and is called as ac conductivity and σ'' is regarded as imaginary part of conductivity, f is the frequency, and ε_0 is the dielectric permittivity of free space.

The complex modulus M^* is given as

$$M^*(f) = M' + jM'' = \frac{\varepsilon'}{\varepsilon'^2 + \varepsilon''^2} + j\frac{\varepsilon''}{\varepsilon'^2 + \varepsilon''^2} \quad (4)$$

The loss tangent, tanδ, is calculated as the ratio of ε'' to ε'. Mathematically, it is expressed as

$$\tan\delta = \frac{\varepsilon''}{\varepsilon'} \quad (5)$$

2.4.4. Scanning Electron Microscopy

Surface micro-images and energy-dispersive X-ray (EDX) spectra of the SPE films were captured using a scanning electron microscopy (SEM) with an EDX detector. The SEM images were scaled and magnified to display the materials' distinctive morphological characteristics, while the EDX spectra provided an elemental analysis of the SPE films.

2.4.5. Atomic Force Microscopy (AFM)

Atomic force microscopy (AFM) topographic images were obtained using Innova AFM in tapping mode. Si (*p*-doped) cantilevers with spring constants of 20–80 Nm^{-1} and resonant frequencies of 250–300 kHz recorded the height images. Measurements were performed at room temperature. Surface roughness was assessed using the root mean square (RMS) height, also known as RMS surface roughness.

2.4.6. Thermal Studies

Heating thermograms of the SPEs were obtained under nitrogen at a flow rate of 40 mL min^{-1} using differential scanning calorimetry (DSC). The temperature range was 30–200 °C with a heating rate of 10 °C min^{-1}. Each sample (around 8 mg) was placed in an aluminum pan with a pierced lid and heated to obtain thermograms (SHIMADZU DSC-60 PLUS). For TGA experiments, samples weighing 5–8 mg were sealed in a 40 µL aluminum can with perforated lids, heated from 30–500 °C at 10 °C min^{-1} (Hitachi STA7200 TGA-DTA). The experiments were conducted under an argon atmosphere to minimize oxidation and ensure a controlled environment.

2.4.7. Linear Sweep Voltammetry

Linear sweep voltammetry (LSV) was conducted using a CH600E galvanostat at a 10 mV s^{-1} scan rate. Sodium amalgam (NaHg) electrodes functioned as both reference and counter electrodes, and stainless steel (SS) electrodes were used as the working electrodes, with SPEs placed between them.

2.4.8. Transference Number Measurements

The transference number measurements (TNM) of all prepared SPE films was measured at 27 °C using a Keithley 2636 B source meter. Electrochemical measurements employed stainless steel (SS) blocking electrodes with an SS|SPE|SS capacitive assembly. TNM experiments lasted 1200 s with a step size of 0.01 s, monitoring current over a period under a constant applied potential of 100 mV to analyze the electrochemical behavior and properties of the SPE films.

The total ionic transference number (t_{ion}) is calculated as follows[22]

$$t_{ion} = 1 - \frac{I_{final}}{I_{initial}} \tag{6}$$

The ionic conductivity (σ_{ion}) was calculated using Equation (7), derived from the bulk conductivity and the transference number

$$\sigma_{ion} = \sigma_{bulk} \times t_{ion} \tag{7}$$

2.4.9. Mechanical Properties

A Dak System Inc. 7200 series device was employed to evaluate the mechanical characteristics, utilizing test specimens conforming to ASTM D880 standards. The specimens had a thickness between 0.1 and 0.2 mm, and the crosshead velocity was set at 0.1 mm min^{-1}. Maintaining a consistent deformation rate during the assessment is essential for obtaining precise measurements of tensile strength, elongation, and modulus. Differences among samples were examined using ANOVA, followed by a post-hoc Tukey test with a 95% confidence interval.

2.5. EDLC Characterization

A two-electrode setup was employed by sandwiching the highest conducting electrolyte between the 2 identical electrodes coated with a mixture of 85 wt% active material, 10 wt% carbon black, and 5 wt% PVDF, which was thoroughly ground to form a homogeneous slurry. This slurry was then applied to stainless steel electrodes with an area of 1 cm^2, and each electrode contained ≈1 mg of active material. Cyclic voltammetry (CV), galvanostatic charging/discharging (GCD), and electrochemical impedance spectroscopy (EIS) measurements (frequency range 1 MHz to 0.01 Hz) were performed using a SP- Biologic 150e electrochemistry workstation.

The C_s of the EDLC was determined from the CV curve using equation

$$C_s = 2\frac{\int Id\nu}{\nu m \Delta V} \tag{8}$$

Specific capacitance (C_s) can be obtained from GCD curve using

$$C_s = 4\ C \tag{9}$$

where C is given by

$$C = \frac{I\,\Delta t}{\Delta V\, m} \tag{10}$$

Here, C represents the capacitance of the EDLC, and m is the mass of the active material in both electrodes. The factor of 4 is used to adjust the cell capacitance to the mass and capacitance of a single electrode, as an EDLC consists of two capacitors, one on each electrode.[23–27]

Further, the energy and power densities were calculated using

$$E = \frac{(\Delta V)^2 C_s}{7200} \tag{11}$$

$$P = \frac{3600 \times E}{\Delta t} \tag{12}$$

where C_s is the specific capacitance (F g^{-1}), i is the discharge current (mA), Δt is the discharge time (s), m is the mass of the active material (g), and ΔV is the effective discharge voltage window.[25,26,28,29]

3. Results and Discussion

3.1. FTIR Spectroscopy Studies

The SPE films had varying compositions that distinguished them from one another based on their unique electrical properties. This was confirmed using FTIR spectroscopy, which allowed for the examination of microscale interactions among functional groups. The examination of peak shape, position, and intensity variations has been utilized to investigate the existence of polymer–ion and ion–ion interactions. Regarding the pure blend, the NaCMC/PVA blend displayed both strong and weak absorption bands attributed to the different functional groups within the polymer as shown in **Figure 1**a. The existence of these bands

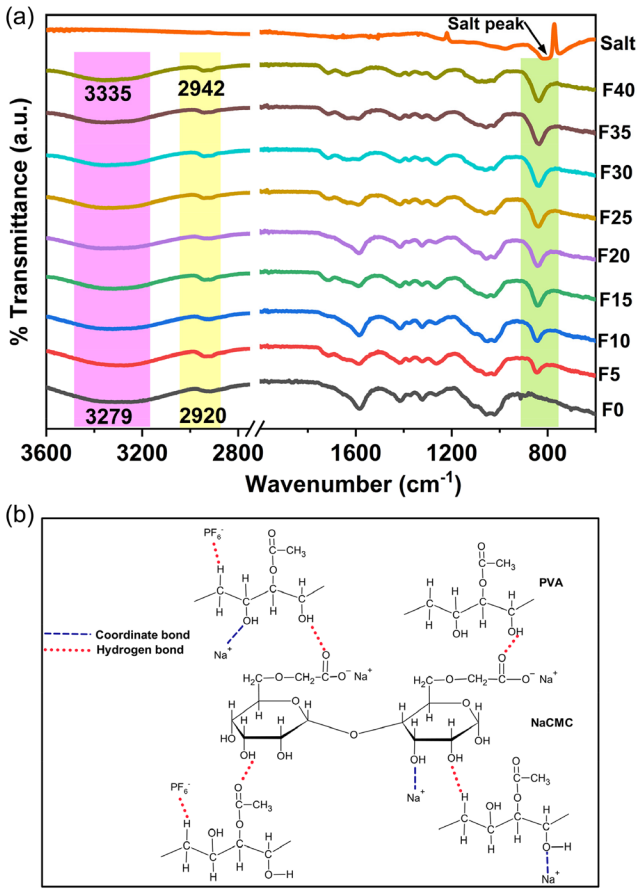

Figure 1. a) FTIR spectra of NaCMC/PVA-$NaPF_6$ SPE and $NaPF_6$ salt and b) probable interaction scheme of the dopant $NaPF_6$ with polymer blend NaCMC/PVA.

aligns with the findings of numerous prior studies.[14,21,30] The major bands are presented in **Table 2**. The characteristic vibrational mode of the PF_6^- anion in the SPE films appeared within the wavenumber range of ≈800–900 cm^{-1}. The asymmetry observed in the peak for all SPE systems could stem from the loss of degeneracy transitioning from octahedral symmetry, which arises because of the simultaneous presence of multiple components, namely, free ions and ion pairs.[31] The introduction of salt into the system resulted in the appearance of an additional band, specifically the C—O—C ether linkage at 834–844 cm^{-1}. The presence of these bands was lacking in the NaCMC/PVA blend, which suggests that they play a role in mediating inter/intramolecular hydrogen bonds between the monomeric units. Their appearance in salt-doped systems suggests that the dopant possesses the ability to disrupt these hydrogen bonds by forming bonds with the polymeric unit.[32]

The variation in the wavenumbers with the systematic incorporation of salt is discussed later. The wavenumber variations considered in our analysis are those that exceed the resolution of the FTIR instrument (4 cm^{-1}), ensuring that the observed shifts are significant and not due to instrumental limitations. The position of the important IR bands has been identified using Spectragryph-optical spectroscopy software version 1.2.14.[33] According to Table 2, the wavenumber associated with the —OH band, ≈3279 cm^{-1} in the pristine blend, shifts toward higher wavenumbers upon salt inclusion. The observed shift indicates a dative bond formation between the cation and the hydroxyl group's oxygen atom. Moreover, alterations in the -CH stretching wavenumber suggest hydrogen bonding between the anion and the —CH group. The wavenumber associated with the C—O—C ether bond also experiences a downward shift, signifying a coordinated bond between the cation and the ether oxygen. This phenomenon is particularly evident, as the cation is attracted to the electron lone pair on the C—O—C group's oxygen atom.[34]

The asymmetry observed in the broad band within the range 800–900 cm^{-1} suggests the presence of two components: a peak attributed to the asymmetric stretching of the PF_6^- anion and another peak corresponding to $Na^+ \ldots PF_6^-$ contact ions.[35,36] Consequently, variations in the intensity of the C—O—C band around 800–900 cm^{-1} were observed with changes in the salt concentration. Thus, the FTIR studies confirmed the interaction of the salt with the polymer blend. The interaction scheme has been given in Figure 1b.

3.2. X-Ray Diffraction Studies

XRD analysis plays a crucial role in assessing the crystalline and amorphous phases within SPE compositions, offering insights

Table 2. FTIR wavenumber assignments for various functional groups in NaCMC/PVA-$NaPF_6$ SPEs.

Functional group	Wavenumber assignments [cm^{-1}]								
	F0	F5	F10	F15	F20	F25	F30	F35	F40
C—O—C ether linkage	–	844	842	843	840	838	835	836	834
C—O—C glycosidic bond	1056	1056	1055	1054	1057	1055	1062	1056	1057
C—H wagging	1266	1263	1268	1266	1266	1265	1269	1271	1267
O—H bending	1322	1322	1324	1323	1324	1324	1325	1324	1323
C—H_2 scissoring	1417	1419	1416	1417	1415	1415	1421	1417	1417
COO^- stretch	1586	1586	1586	1589	1588	1592	1586	1590	1590
C=O Stretch	1715	1715	1717	1712	1712	1721	1717	1716	1716
C—H stretching	2920	2941	2921	2942	2943	2944	2944	2941	2942
O—H stretch	3279	3262	3249	3312	3372	3353	3334	3356	3335

into shifts in peak position, broadening, and intensity reduction. **Figure 2**a displays the XRD spectra of NaCMC/PVA doped with $NaPF_6$ across different compositions, providing insights into the microstructure of these SPEs based on peak and intensity variations. The semi-crystalline structure of the NaCMC/PVA blend was evidenced by the presence of a prominent diffraction peak at $\approx 2\theta = 20°$, indicating the coexistence of crystalline and amorphous regions within the material.[9] Furthermore, this broad peak has been consistently observed in the XRD patterns of NaCMC/PVA in previous studies.[21]

The diffraction pattern of $NaPF_6$ shows clear, well-defined peaks at $2\theta = 23.3°$, 20.18°, and several others, which is indicative of its crystalline nature, as confirmed by its JCPDS card number 96-152-1417. It is worth noting that no salt-associated peaks were observed, thus suggesting complete dissociation within the polymer. According to Figure 2a, there was a reduction in the relative intensity of the broad peak as the salt content increased, observed within the range of 10°–50°. This may be attributed to the inter-/intra-interactions between NaCMC/PVA and $NaPF_6$.

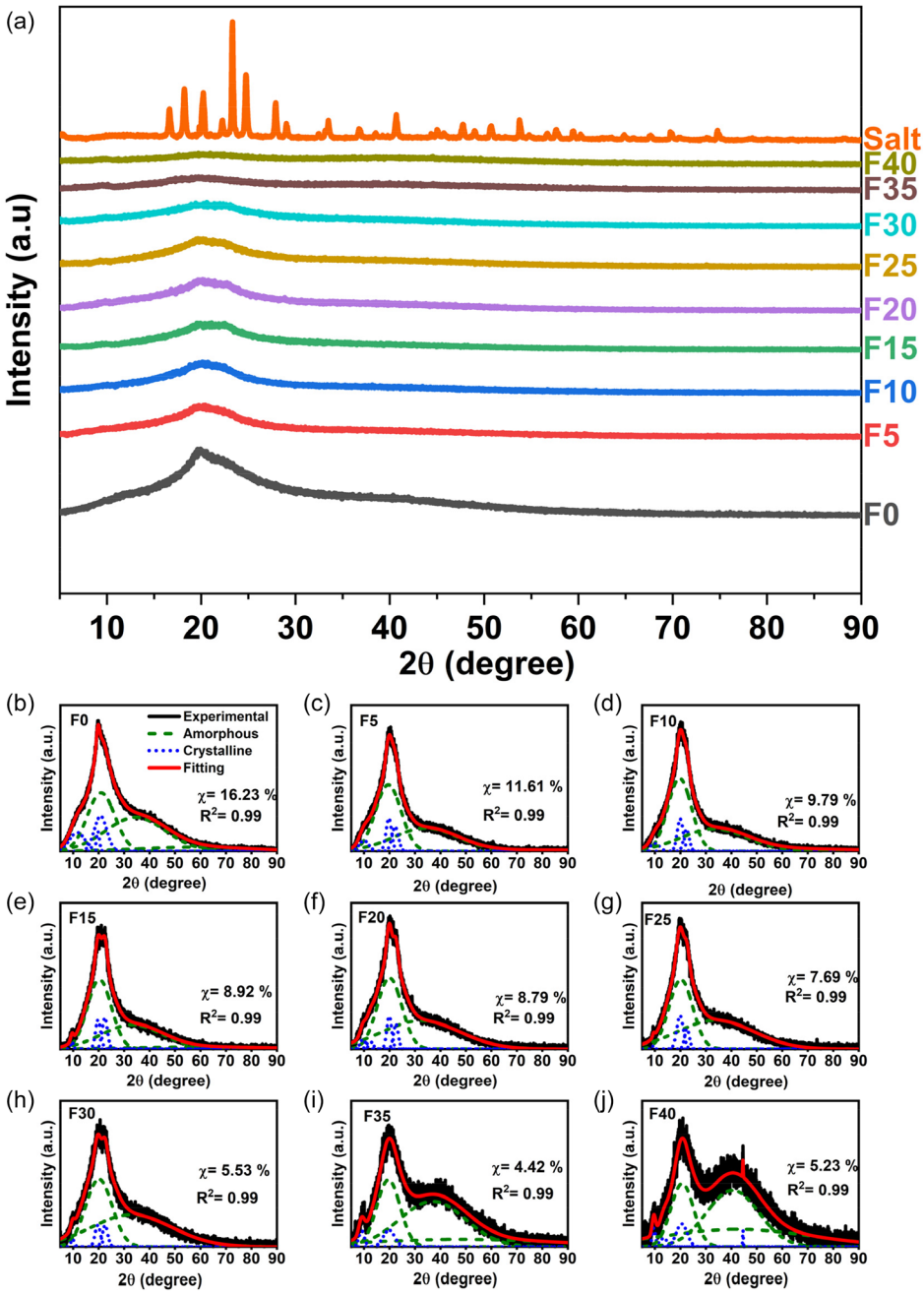

Figure 2. a) XRD spectra of the NaCMC/PVA-$NaPF_6$ SPEs along with XRD spectra of $NaPF_6$ salt, b–j) deconvoluted XRD spectra for NaCMC/PVA-$NaPF_6$ SPEs.

Bond breaking and bond-forming processes result in an increase in the amorphousness of the SPEs system, as evidenced by IR studies.[37] The optimal conducting electrolyte system typically displays a broad peak, which is often in the form of an amorphous hump. The intensity and breadth of the peaks are thought to be a result of the complexation between the polymer and the dopant, which is facilitated by the formation of hydrogen or dative bonding within the CMC/PVA-$NaPF_6$ solid biopolymer electrolyte system. This process ultimately leads to the creation of a more amorphous region within the polymer matrix.[38] As the ion concentration in the SPEs system rises, a corresponding increase occurs in both the fractions of the amorphous phase and charge carriers.[39] The observation of an increase in the amorphous phase can be inferred from the reduction in peak intensity and broadening of the peak, as indicated by Hodge et al.[40] Therefore, the F35 and F40 samples were the most amorphous of all the doped samples.

The deconvolution technique is a useful addition to the XRD analysis of polymer electrolytes, as it allows for a clearer understanding of their amorphous nature. By applying this method, the XRD patterns become more precise, making it easier to examine the crystallinity and amorphous peaks, especially when the patterns are overlapping in the spectra.[14] Cohen suggests that amorphous peaks typically exhibit broad characteristics, contrasting with the sharp and narrow reflections of crystalline phases.[41] In Figure 2b-j, the deconvoluted diffractograms of all tested SPEs are depicted, with a baseline correction applied before fitting using a Gaussian distribution. The criteria for assigning crystalline and amorphous peaks along with the baseline correction method have been outlined in our previous work to ensure minimal errors during fitting procedure.[16,17] The degree of crystallinity of the samples was evaluated using the following Equation (13)

$$\chi = \frac{\text{area under all crystalline peaks}}{\text{area under all peaks}} \times 100\% \tag{13}$$

The calculations revealed that the pure blend possessed a crystallinity of 16.23%, which began to diminish with the addition of salt. This suggests that $NaPF_6$ completely dissolved in the SPEs, rendering them more amorphous. Both inter- and intra-molecular attractions facilitated this dissolution process, as evidenced by IR analysis. As the salt concentration increased, so did the number of amorphous peaks, indicating a higher level of disorder in the material's structure. This transformation is crucial for understanding changes in ionic conductivity, as a greater presence of amorphous regions typically enhances ion mobility. Among the prepared SPEs, F35 demonstrated the lowest crystalline percentage at 4.42%, attributed to its extended broadness and reduced peak intensity. Consequently, a more amorphous sample encounters a lower energy barrier for conduction, resulting in improved ionic conductivity of the F35 sample. This observation aligns with the ionic conductivity trend, which primarily depends on the movement of mobile carriers that occur more freely in amorphous regions.[13] Additionally, the addition of salt in amounts exceeding 35 wt% led to ion reassociation, consequently increasing crystallinity to 5.23%, and decreasing ionic conductivity.[42]

3.3. Electrochemical Impedance Spectroscopy

Figure 3 displays Nyquist plots depicting the imaginary impedance plotted against the real impedance for the NaCMC/PVA-$NaPF_6$ SPE films. The Nyquist plot of the film showed a depressed semicircle coupled with a tilted spike. The capacitive effect that is characterized by a low-frequency spike and a high-frequency arc in the complex impedance plots is commonly found in double-layer capacitors. This effect is usually attributed to two factors: the accumulation of charges at the electrolyte–electrode interface and the bulk conduction process. Instead of the expected vertical spike in the impedance plot (see Figure S1a, Supporting Information), an inclined spike with an angle of less than 90° was observed, suggesting nonideal capacitance (see Figure S1b, Supporting Information). This deviation may stem from non- homogeneity or roughness at the electrolyte–electrode interface. Bulk resistance can be determined by locating the intercept of the high-frequency semicircle on the Z' -axis. The impedance data were analyzed by fitting it with a theoretical simulation using an electrical equivalent circuit (EEC) arrangement. In the high-frequency range, the impedance of the system is characterized by a parallel connection of R_b (the bulk resistance) and CPE (constant phase element). In contrast, in the low-frequency range, CPE dominates, suggesting the formation of an electric double-layer between the electrodes and electrolyte.[43] The impedance of the CPE is given by $Z_{CPE} = \frac{k}{(j\omega)^p}$, where k^{-1} is the CPE capacitance, and p ($0 < p < 1$) indicates how much the spike deviates from the vertical axis in the Nyquist plot.[44]

The impedance of the equivalent circuit is given by Equation (14).

$$Z^* = Z' + j(-Z'') = \frac{R_b}{1 + R_b k_1^{-1} (j\omega)^{p_1}} + \frac{k_2}{(j\omega)^{p_2}} \tag{14}$$

Simplifying Equation (14), yields Equation (15) and (16).

$$Z' = \frac{R_b + R_b^2 k_1^{-1} \omega^{p_1} \cos(\frac{\pi p_1}{2})}{1 + 2R_b k_1^{-1} \omega^{p_1} \cos(\frac{\pi p_1}{2}) + R_b^2 k_1^{-2} \omega^{2p_1}} + \frac{\cos(\frac{\pi p_2}{2})}{k_2^{-1} \omega^{p_2}} \tag{15}$$

$$-Z'' = \frac{R_b^2 k_1^{-1} \omega^{p_1} \sin(\frac{\pi p_1}{2})}{1 + 2R_b k_1^{-1} \omega^{p_1} \cos(\frac{\pi p_1}{2}) + R_b^2 k_1^{-2} \omega^{2p_1}} + \frac{\sin(\frac{\pi p_2}{2})}{k_2^{-1} \omega^{p_2}} \tag{16}$$

From Figure 3, it is evident that the impedance of the theoretical equivalent circuit aligns seamlessly with experimental impedance data. The bulk conductivity (σ_{bulk}) has been calculated using equation

$$\sigma_{bulk} = \frac{t}{R_b A} \tag{17}$$

Here t is the thickness and A is the effective area of contact, R_b is the bulk resistance. The parameters such as R_b, σ_{bulk} obtained from the EEC analysis have been tabulated in **Table 3**.

The F35 sample had the lowest bulk resistance value and the highest bulk conductivity of $(2.26 \pm 0.19) \times 10^{-5}$ S cm^{-1} at room temperature. As the concentration of salt increased, conductivity decreased due to the phenomenon of salt reassociation. The conductivity of the optimum sample is quite low when compared to state-of-the-art electrolytes (mS cm^{-1} at

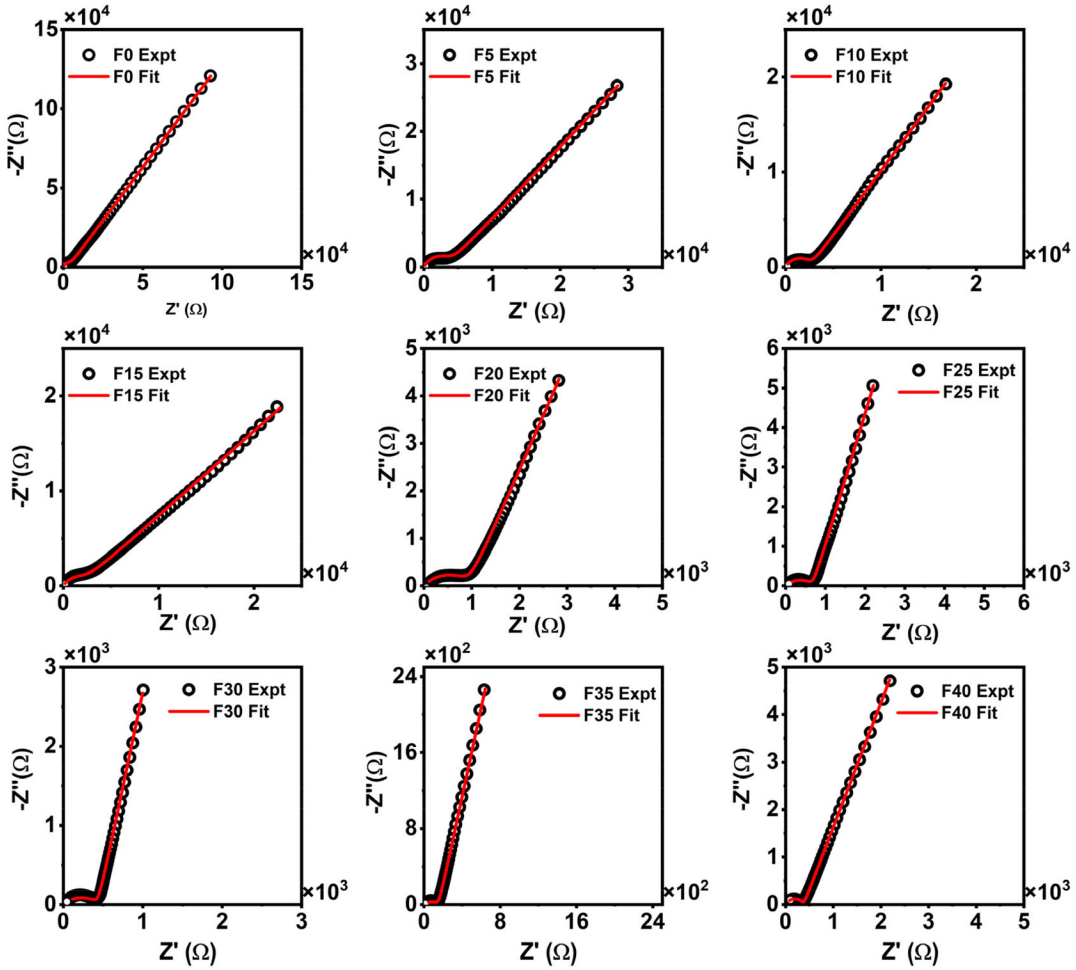

Figure 3. Nyquist plot for NaCMC/PVA-$NaPF_6$ SPEs (black circles represent the experimental data points and red line represent the fitted data points).

Table 3. Variation in bulk resistance by EEC modeling R_b, bulk conductivity σ_{bulk}, dc conductivity $\sigma_{dc}$from ac conductivity, JPL fitting parameters B, s along with regression coefficient R^2, and condutiivty relaxation time τ for NaCMC/PVA-$NaPF_6$ SPEs.

Sample	R_b[Ω]	σ[S cm^{-1} at 25 °C]	σ_{dc} at 25 °C [S cm^{-1}]	B	s	(τ) [s]	R^2
F0	3502.57 ± 342.50	$(5.42 \pm 0.52) \times 10^{-7}$	$(2.79 \pm 0.13) \times 10^{-7}$	$(2.31 \pm 0.87) \times 10^{-12}$	0.89 ± 0.02	–	0.99
F5	3285.72 ± 54.92	$(9.45 \pm 0.15) \times 10^{-7}$	$(8.95 \pm 0.22) \times 10^{-7}$	$(1.78 \pm 0.34) \times 10^{-12}$	1 ± 0.01	2.00×10^{-4}	0.99
F10	2637.50 ± 40.79	$(1.68 \pm 0.02) \times 10^{-6}$	$(1.19 \pm 0.20) \times 10^{-6}$	$(4.46 \pm 3.39) \times 10^{-12}$	1 ± 0.04	5.65×10^{-5}	0.97
F15	1833.33 ± 124.72	$(2.80 \pm 0.18) \times 10^{-6}$	$(1.57 \pm 0.04) \times 10^{-6}$	$(2.82 \pm 0.75) \times 10^{-12}$	1 ± 0.01	2.05×10^{-5}	0.99
F20	1041.67 ± 65.68	$(3.90 \pm 0.24) \times 10^{-6}$	$(3.43 \pm 0.32) \times 10^{-6}$	$(1.39 \pm 1.01) \times 10^{-11}$	1 ± 0.04	1.12×10^{-5}	0.97
F25	725.83 ± 14.26	$(9.59 \pm 0.59) \times 10^{-6}$	$(9.97 \pm 0.17) \times 10^{-6}$	$(7.55 \pm 11.81) \times 10^{-12}$	1 ± 0.09	2.83×10^{-6}	0.91
F30	487.06 ± 28.34	$(1.33 \pm 0.07) \times 10^{-5}$	$(1.26 \pm 0.06) \times 10^{-5}$	$(8.68 \pm 13.61) \times 10^{-8}$	1 ± 0.10	4.48×10^{-6}	0.90
F35	162.54 ± 9.08	$(2.26 \pm 0.19) \times 10^{-5}$	$(2.41 \pm 0.12) \times 10^{-5}$	$(1.14 \pm 2.70) \times 10^{-7}$	1 ± 0.15	2.52×10^{-6}	0.86
F40	372.76 ± 21.16	$(1.95 \pm 0.11) \times 10^{-5}$	$(1.71 \pm 0.03) \times 10^{-5}$	$(8.76 \pm 4.15) \times 10^{-9}$	0.49 ± 0.02	1.59×10^{-6}	0.98

room temperature) reported in literature. However, integrating plasticizers or ionic liquids offers a promising route to achieve this conductivity enhancement by increasing ionic mobility within the polymer matrix.

The rise in conductivity has been assessed by examining transport properties, using parameters obtained from fitting the Nyquist plot.[45] The following equations are utilized to determine transport parameters

$$D = \frac{e(k_2\varepsilon_r\varepsilon_0 A)^2}{\tau_2} \tag{18}$$

$$\mu = \frac{eD}{k_B T} \tag{19}$$

$$n = \frac{\sigma}{\mu e} \tag{20}$$

The variation in the room temperature transport parameters for the NaCMC/PVA blend doped with various concentrations of $NaPF_6$ is illustrated in **Figure 4**.

The conductivity of the NaCMC/PVA-$NaPF_6$ electrolytes at room temperature increased with the inclusion of salt and reached its peak value of $(2.26 \pm 0.19) \times 10^{-5}$ S cm^{-1} for the F35 electrolyte. However, as the salt concentration surpassed 35 wt%, conductivity experienced a decline. The trend in charge carrier concentration corresponds with the pattern observed in conductivity. Also, charge carrier mobility and diffusion coefficient exhibit same relationship to conductivity. This suggests that carrier concentration has significant impact on conductivity along mobility and diffusion coefficient. In the F30 and F35 samples, the higher carrier concentration resulted in reduced mobility and diffusion coefficient, as there was less space available for free ion movement. For the F40 sample, the ion association caused a notable reduction in carrier concentration, leading to a decrease in ionic conductivity.

3.4. AC Conductivity Studies

Electrical conduction through electrolytes is characterized by log–log plots of $\sigma' = \sigma_{ac}$, the real part of the complex conductivity, versus frequency at room temperature, as illustrated in **Figure 5**a, which depicts three distinct regions. In the low-frequency range, σ' decreases as frequency decreases. This phenomenon is often attributed to the fluctuation of interfacial polarization at the electrode–sample interface. The primary function of the electrode is to create a layered separation of positive and negative charges, which is primarily capacitive in nature. This region has restricted conductivity because the electric field in this area opposes the applied electric field. At higher frequencies, there is a plateau of nearly frequency-independent conductivity known as dc conductivity (σ_{dc}). The dispersive region in the high-frequency domain, characterized by frequency-dependent conductivity, extends beyond this plateau and could offer insights into the chemical environment within the material.[46]

The transition from the plateau region to the dispersive region can be characterized using an empirical power law, known as the universal dynamic response, first proposed by Jonscher. This can be described as follows

$$\sigma_{ac} = \sigma_{dc} + Bf^s \tag{21}$$

where f represents the frequency of the applied electric field, and B and s are fitting parameters with an empirical nature. Parameter "s" is defined as

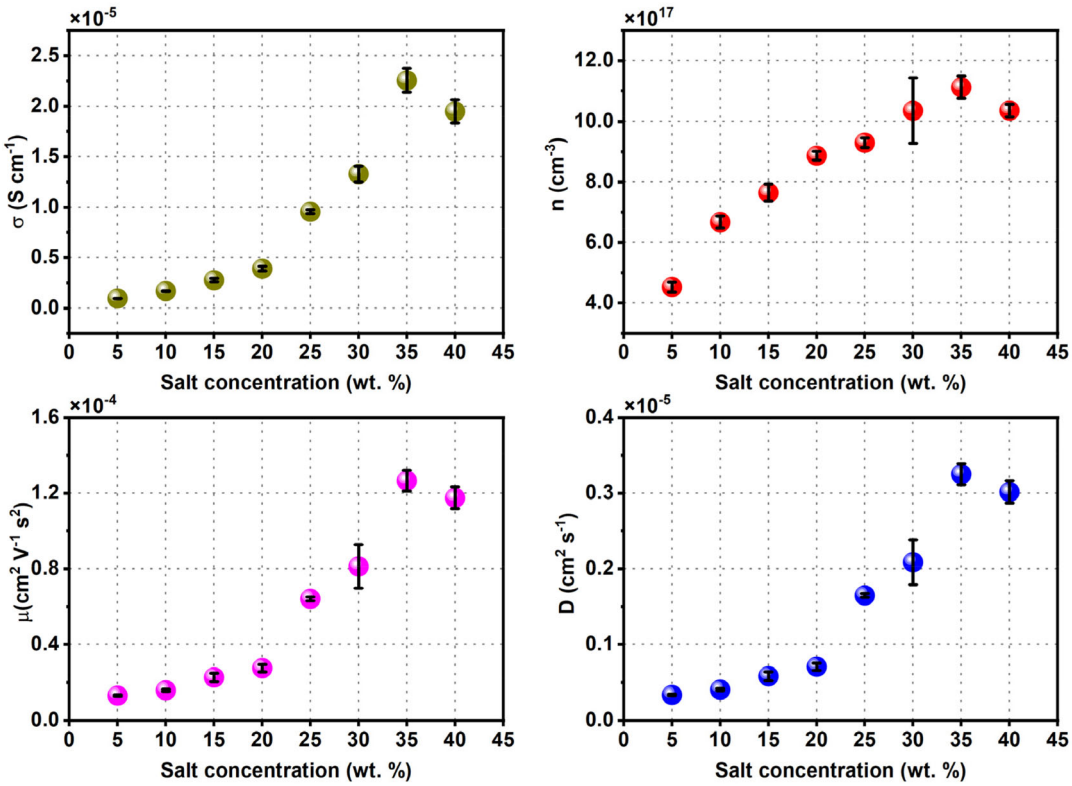

Figure 4. Room temperature ion transport properties calculated from Nyquist plot fitting for NaCMC/PVA-$NaPF_6$ SPEs.

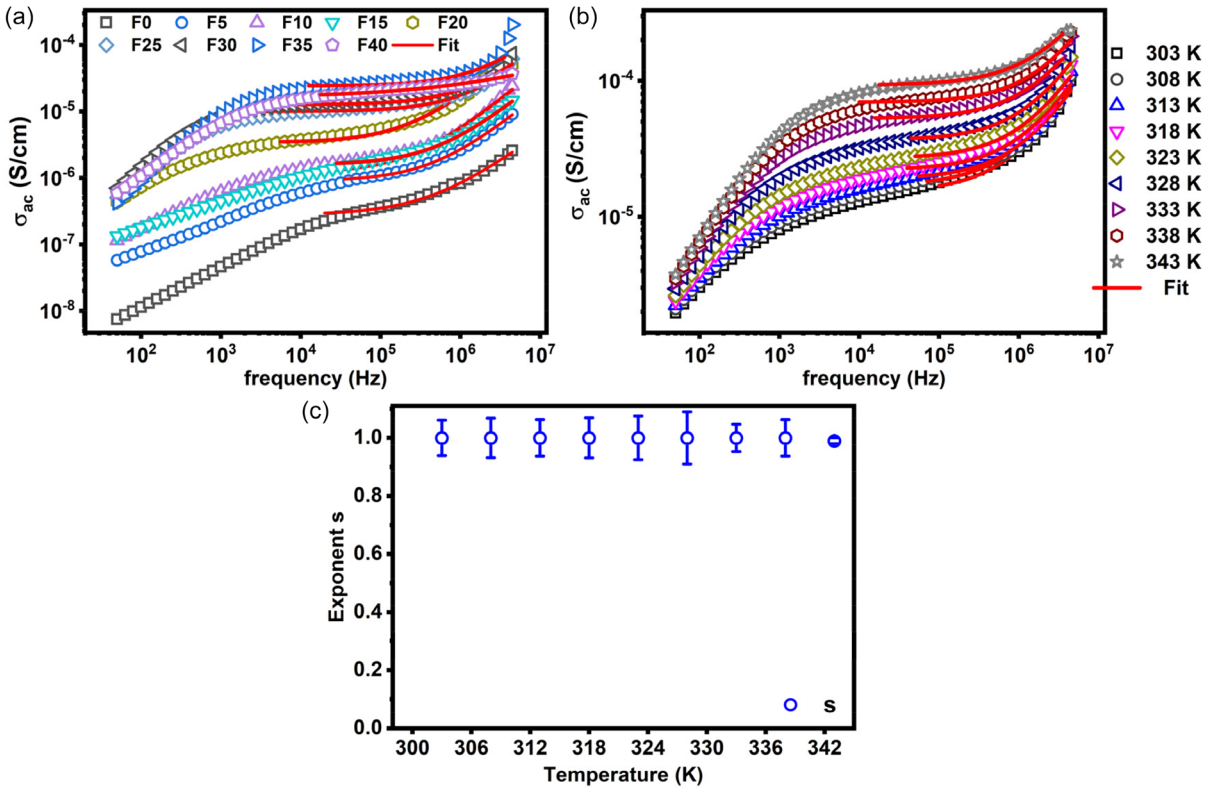

Figure 5. a) Room temperature AC conductivity spectra, b) high-temperature AC spectra of F35 SPE, and c) variation in the Jonscher power exponent 's' for F35 SPE for temperature 308–343 K.

$$s = \frac{\text{backhope rate}}{\text{site relaxation time}} \tag{22}$$

The movement of Na^+ ions occur at a slower pace when the value of "*s*" is less than one, as the backward hop is slower than the site relaxation. Typically, "*s*" ranges between zero and unity, although exceptions with $s > 1$ have been observed. The room-temperature data were fitted using Equation (21), and the fitting parameters are listed in Table 3. The values for conductivity obtained through fitting method align with those obtained from the Nyquist plot formalism, and the value of "*s*" falls within the range of 0.29–1 for the salt-doped samples. Additionally, "*s*" is influenced by temperature. According to Mauritz's research on ion hopping in hydrated Nafion membranes, "*s*" is indicative of the connectivity of long-range charge hopping pathways or the degree of tortuosity for mobile charges.[47] Figure 5b,c represents the high-temperature ac conductivity plot and variation of parameter "*s*," respectively, for F35 sample for the temperature range 303–343 K. Several theoretical models have been proposed to explain the connection between the exponent "*s*" and temperature in polymer electrolytes, providing valuable understanding of the conduction mechanism in these materials. The most notable models include: 1) quantum mechanical tunnelling (QMT), where the exponent "*s*" remains unchanged as temperature increases; 2) small polaron quantum mechanical tunnelling (SP), in which the exponent "*s*" rises with temperature; 3) correlated barrier hopping, where the exponent "*s*" declines as temperature increases; and 4) overlapping large polaron quantum mechanical tunnelling (OLP), where the exponent "*s*" initially decreases with temperature, then begins to increase after reaching a certain point.[42] Examining how "*s*" changes with temperature and comparing it to theoretical models allows scientists to obtain crucial information about the dominant conduction mechanism in the polymer electrolyte system. Nevertheless, when temperatures exceeded 343 K, the Jonscher fit failed to converge, making it impossible to determine the value of "*s*". The inability of the Jonscher Power Law fit to converge at temperatures above 343 K was probably due to the lack of a high-frequency dispersion region in the collected data. Our research indicates that the F35 sample follows the QMT model for conduction throughout the examined temperature range, as evidenced by the constant value of "*s*" at 1, which is unaffected by temperature changes.

3.5. Dielectric Analysis

The complex permittivity of a material is comprised of two components: a real part ε', which represents the stored energy, and an imaginary part ε'', which signifies the energy loss resulting from periodic field reversals (**Figure 6**a,b). The values of the ε' for these electrolytes are in the thousands at low frequencies, dropping nonlinearly as the frequency increases, and approaching a constant level (ε_∞) around 1 MHz. The spectra of ε' reveal a point of inflection around 1 kHz, suggesting that the ε'values at this

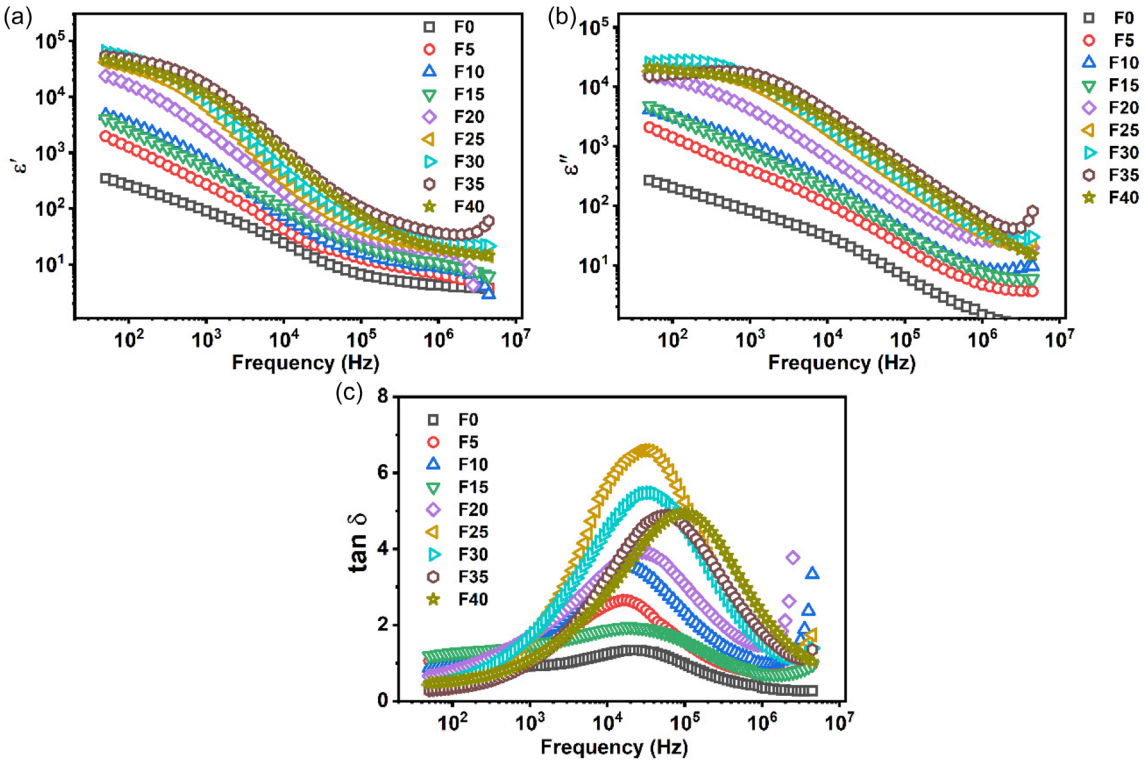

Figure 6. Variation in room temperature a) real permittivity, b) imaginary permittivity, c) tangent loss for NaCMC/PVA-$NaPF_6$ SPEs.

frequency can be regarded as the static permittivity (ε_s) of the electrolytes. The inflection point observed at this frequency likely indicates a transition in the dielectric response of the material, which could be associated with a change in the dominant polarization mechanism. Below 1 kHz, the polarization is primarily due to dipole orientation, which contributes significantly to the overall permittivity. As the frequency increases beyond this point, the dipoles may not align as effectively with the alternating field, leading to a decrease in ε', hence the observed inflection. The values of the static permittivity (ε_s) and the high frequency limiting permittivity (ε_∞) of the polymeric electrolytes obtained graph of frequency-dependent real permittivity and imaginary permittivity with different salt concentrations are provided in **Table 4**. Additionally, the dielectric strength ($\Delta\varepsilon = \varepsilon_s - \varepsilon_\infty$) of these samples has been listed in Table 4.

Based on the data presented in Table 4, it is evident that the dielectric strength increased with the addition of salt. This trend could be attributed to the complete dissociation of the salt owing to polymer–ion interactions, leading to a high free ion concentration. The high dielectric constant ε_s observed further supports this conclusion.[48] The F35 sample demonstrates the highest dielectric strength $\Delta\varepsilon$, which suggests that it also possesses the highest ionic conductivity. This implies that at this concentration, the maximum quantity of salt dissociates into cations and

Table 4. Values of ε_s, ε_∞, dielectric strength $\Delta\varepsilon$, calculated graph of ε' and ε'' at room temperature for NaCMC/PVA-$NaPF_6$ SPEs.

	Parameter from ε'			Parameter from ε''		
Sample	ε_s	ε_∞	$\Delta\varepsilon = \varepsilon_s - \varepsilon_\infty$	ε_s	ε_∞	$\Delta\varepsilon = \varepsilon_s - \varepsilon_\infty$
F0	89.69 ± 0.49	4.23 ± 0.01	85.46 ± 0.49	82.40 ± 0.38	1.48 ± 0.01	80.93 ± 0.37
F5	268.77 ± 0.51	6.67 ± 0.01	262.11 ± 0.51	395.62 ± 1.29	4.72 ± 0.01	390.90 ± 1.28
F10	710.08 ± 1.03	8.77 ± 0.03	701.31 ± 1.00	1100.76 ± 5.31	8.37 ± 0.31	1092.39 ± 4.99
F15	543.59 ± 3.41	10.58 ± 0.01	533.01 ± 3.41	796.85 ± 4.21	7.68 ± 0.02	789.17 ± 4.19
F20	2478.20 ± 3.02	18.33 ± 0.38	2459.87 ± 3.40	4160.11 ± 53.79	24.96 ± 1.41	4135.16 ± 52.38
F25	6432.56 ± 32.26	22.87 ± 0.03	6409.70 ± 32.24	10807.50 ± 47.13	54.33 ± 0.25	10753.17 ± 47.37
F30	8360.63 ± 620.47	26.22 ± 0.29	8334.41 ± 620.76	14972.24 ± 95.81	40.84 ± 0.74	14931.40 ± 96.55
F35	16834.63 ± 109.98	36.67 ± 0.12	16797.96 ± 109.86	16565.29 ± 118.55	66.01 ± 0.24	16499.28 ± 118.32
F40	11013.16 ± 28.40	19.66 ± 0.03	10993.50 ± 28.43	11897.33 ± 32.41	45.65 ± 0.04	11851.69 ± 32.37

anions. Consequently, the polarization related to the dielectric strength is heightened.[35] The decrease in the dielectric strength $\Delta\varepsilon$ and ε_s of the F40 sample indicated that the electrolyte failed to accumulate more ions, resulting in ion overcrowding and a reduction in ion density.

The loss-tangent plot is shown in Figure 6c. The graph shows a characteristic peak indicating ionic conduction within the current system. At low frequencies, the graph shows an increase in loss, which can be attributed to the dominance of the Ohmic component over the capacitive element. The alignment of molecular rotation frequency with a specific peak frequency facilitates the maximum transfer of power to the dipoles, resulting in the highest possible heat generation. At high frequencies, the capacitive element becomes prevalent, while the resistive part remains constant, and the capacitive part increases with frequency. The current investigation aimed to explore the impact of salt concentration. As can be seen in the Figure 6c, the relaxation peak moves toward the higher frequency end, which suggests that the ions move more rapidly between the coordinating sites owing to a shorter relaxation time and higher mobilities.

The conductivity relaxation time (τ) is calculated by using the frequency of the maxima f_m and has been listed in Table 3.

$$\tau = \frac{1}{2\pi f_m} \tag{23}$$

The polymer salt complex demonstrating the highest bulk conductivity (F35) also showed the maximum relaxation frequency. A reduced τ value indicates increased flexibility in the polymer chains, enabling more effective movement of charge carriers through the polymer matrix.[49]

Typically, polymers with low polarity exhibit ε' values that remain stable across temperature ranges, whereas highly polar polymers show an increase in ε' as temperatures rise. The observed pattern in ε' from the current studies aligns with the behavior of polar dielectric materials, where higher temperatures enable dipoles to orient more easily, resulting in enhanced dielectric permittivity. The temperature-dependent variation in the dielectric spectra for the F35 sample is detailed below (Figure S2a,b, Supporting Information).

It is observed that both (ε') and (ε'') values increase with rising temperature. This increase is attributed to the higher charge density and additional contributions from interfacial polarization. This is evident by the increasing value of $\Delta\varepsilon$ with the temperature (**Table 5**). As the temperature increases, ε' and ε'' are found to increase because more ions are made available as $NaPF_6$ dissociates into Na^+ and PF_6^- with the supply of thermal energy, as supported by the following equation.

$$n = n_0 \exp\left(-\frac{U}{k_b T}\right) \tag{24}$$

Equation (24) shows that n represents the density of free ion carriers, U denotes the energy required for salt dissociation, and T stands for the absolute temperature. Within the specified temperature range, the lack of a notable relaxation peak in the ε'' graph suggests that the polymer does not undergo any significant primary or secondary structural relaxation processes.

The tangent loss graph (Figure S2c, Supporting Information) across the specified temperature range displays a single, asymmetrical peak, indicative of conductivity relaxation. The peak's asymmetry suggests deviation from the Debye model. Additionally, the peak shifts to higher frequencies and grows in size, signifying reduced relaxation time and increased carrier concentration with rising temperature.

Figure S2d, Supporting Information, depicts the tangent loss for F35 on scaled coordinates, namely $\tan\delta/\tan\delta_{max}$ versus f/f_{max} at different temperatures, where f_{max} denotes the frequency at which the tangent loss, $\tan\delta_{max}$, reaches its maximum. The data for the dielectric loss forms a single master curve, except for inconsistencies at lower frequencies. These low-frequency discrepancies are due to electrode polarization (EP). The tangent loss scaling implies that the conduction process is consistent across various temperatures, indicating a uniform mechanism within the specified temperature range.

3.6. Modulus Spectra Analysis

Figure 7a,b, shows the electric modulus (M' and M'') for NaCMC/PVA-$NaPF_6$ SPEs. The polarization effect of electrodes does not have any effect on the spectra, and it remains consistent regardless of the type of electrode material, the contact between the electrode and the dielectric sample, or any impurities that may be present in the sample. The real (M') and imaginary parts (M'') of the spectra for these electrolytes show dispersion above 100 kHz. In regions where the EP effect is dominant, the values approach zero due to the product $M^*(f) \times \varepsilon^*(f) = 1$. Typically, the M'' spectra of ion-conducting electrolytes display a peak that corresponds to the relaxation time of ionic conductivity. However, the peaks in the M'' spectra of these electrolytes seem

Table 5. Values of static permittivity ε_s, high-frequency limiting permittivity ε_∞, dielectric strength calculated graph of ε' and ε'' for F35 sample from 303 to 353 K.

	Parameter from ε'			Parameter from ε''		
Temperature [K]	ε_s	ε_∞	$\Delta\varepsilon = \varepsilon_s - \varepsilon_\infty$	ε_s	ε_∞	$\Delta\varepsilon = \varepsilon_s - \varepsilon_\infty$
303	6175.92 ± 12.74	43.27 ± 0.03	6132.65 ± 12.72	14440.61 ± 27.26	54.13 ± 0.08	14386.39 ± 27.18
313	7892.41 ± 36.92	46.15 ± 0.06	7846.26 ± 36.86	18015.01 ± 86.83	64.52 ± 0.24	18037.33 ± 86.59
323	12050.05 ± 98.82	50.79 ± 0.09	11999.25 ± 98.73	25899.54 ± 178.21	86.00 ± 0.48	25813.54 ± 177.73
333	27000.90 ± 315.04	56.90 ± 0.03	26944.00 ± 315.01	47819.06 ± 402.36	148.78 ± 1.20	47670.28 ± 401.16
343	51809.73 ± 1019.88	51.34 ± 0.50	51758.38 ± 1020.38	74508.21 ± 955.36	239.43 ± 3.57	74268.79 ± 951.79
353	97113.67 ± 1081.35	8.60 ± 1.47	97105.07 ± 1082.82	108302.90 ± 660.45	401.91 ± 3.87	107901.00 ± 656.58

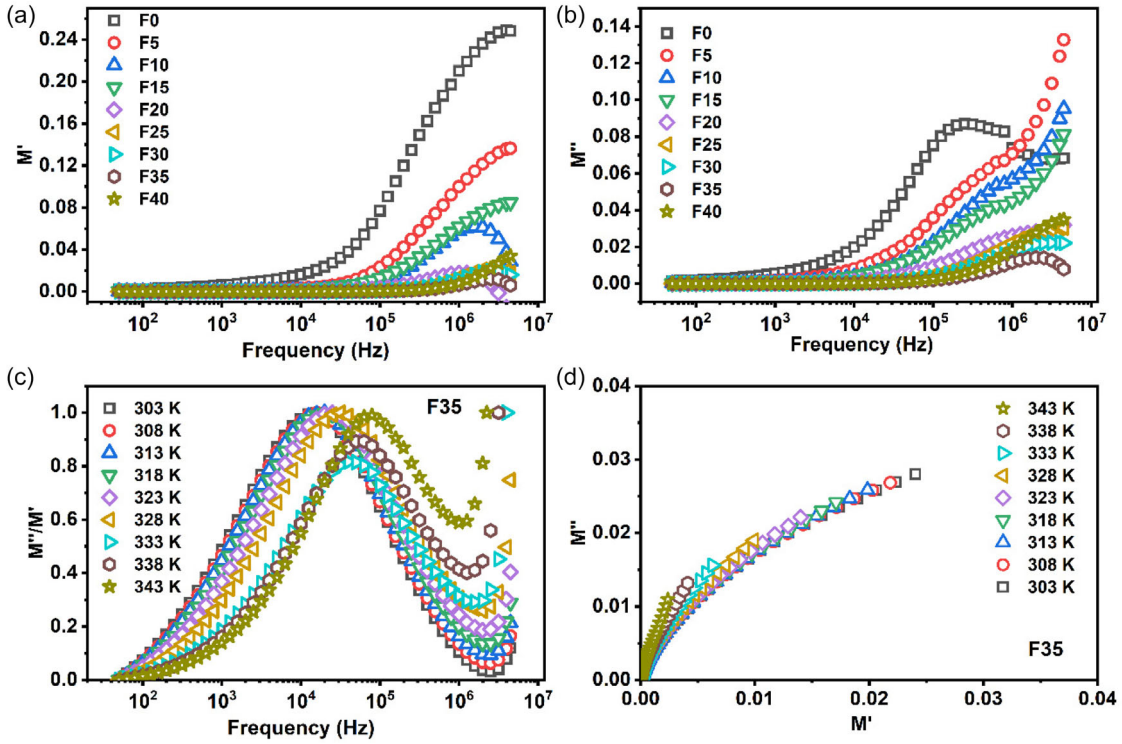

Figure 7. Variation of room temperature a) M′, b) M″ for NaCMC/PVA-$NaPF_6$ SPEs c) high temperature normalized modulus, d) high-temperature Argand diagram for F35 sample.

to be beyond the upper limit of the experimental frequency range. As the temperature increases, the dispersion of the imaginary part shifts toward higher frequencies, indicating that the ionic relaxation is thermally activated and involves the movement of charge carriers.

The asymmetry evident in the M''/M' curves (Figure 7c) indicates that the Kohlrausch–Williams–Watts (KWW) function serves as an appropriate model for representing the relaxation time distribution in polymer electrolytes. This function is frequently employed to illustrate nonexponential patterns in relaxation processes. The dielectric modulus is given by

$$M^* = M_\infty \left[1 - \int_0^\infty \mathrm{d}t e^{-i\omega t}\left(\frac{\mathrm{d}\phi}{\mathrm{d}t}\right)\right] \tag{25}$$

$$\phi(t) = e^{\left[-\frac{t}{\tau_\infty}\right]^\beta} \tag{26}$$

where t_∞ and β are the conductivity relaxation time and KWW exponent. The β value corresponding to F35 SPE was in the range 0.51–0.66 indicating non-Debye nature of the relaxation process.

Argand diagrams clearly depict an incomplete semicircle, indicating a deviation from Debye relaxation (Figure 7d). This non-Debye behavior is attributed to multiple polarization mechanisms and interactions between ions and dipoles within the material, leading to a distribution of relaxation times. As resistivity decreases, the curve deviates further from the semicircular shape, becoming more distorted with rising temperature and causing the tail to approach the imaginary axis. A semicircular Argand plot suggests conductivity relaxation, while deviations indicate viscoelastic or polymer molecular relaxation. Additionally, the semicircle diameters falling significantly below the real axis point to a distribution of relaxation times and ion transport due to viscoelastic relaxation processes.

3.7. Scanning Electron Microscopy

The compatibility between various components of polymer electrolytes is often examined using scanning electron microscopy, which can reveal signs of phase separation and interfaces. The morphology of the pure NaCMC-PVA blend and selected $NaPF_6$-doped blend samples is shown in **Figure 8** at 2500× magnification. The F0 blend sample displayed a uniform morphology without any visible phase separation, suggesting compatibility between NaCMC and PVA components. The introduction of salt resulted in a smoother surface with micropores, which gradually combined to form larger globules. Notably, electrolytes with smooth surfaces facilitate unimpeded movement of conducting ions, leading to higher conductivity values. Additionally, smooth-surfaced polymer electrolytes improve electrode contact, enhance interface stability and decrease resistance.[50] Moreover, the smooth surface of the polymer electrolyte minimizes dendrite formation, thereby enhancing its overall effectiveness.[51] At a salt concentration of 40 wt%, the surface transitions from smooth to exhibiting white spots or patches, signaling the beginning of salt aggregation. The EDAX spectra of F35 revealed essential elements such as Na, P, and F, confirming the successful incorporation of salt into the matrix.

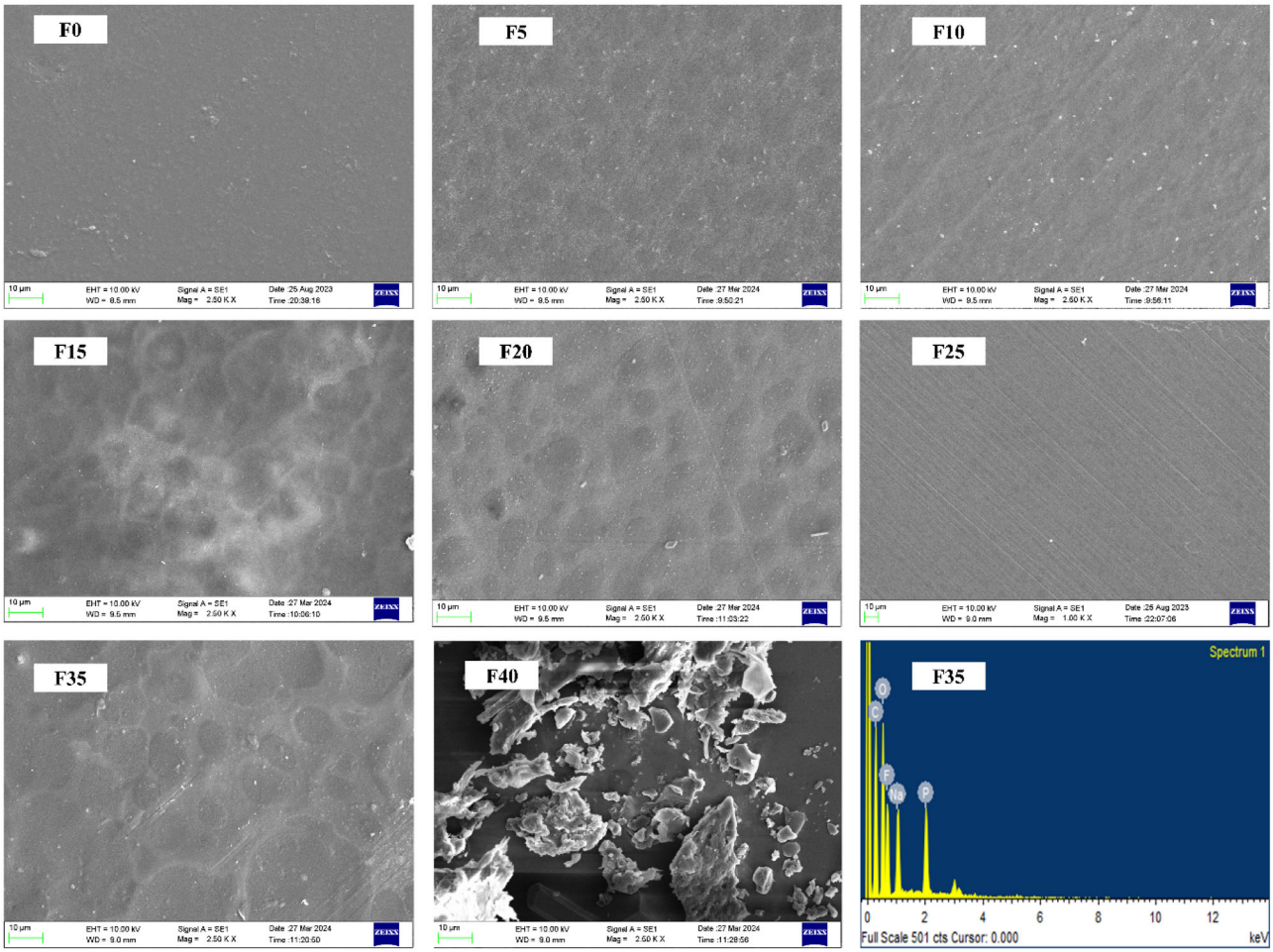

Figure 8. SEM micrographs of selected NaCMC/PVA-$NaPF_6$ SPE along with EDAX spectra (bottom right) for the F35 sample.

3.8. Atomic Force Microscopy

Figure 9 presents the AFM 2D and 3D topographic images of F0, F35, and F40 samples. The NaCMC/PVA-$NaPF_6$ system images well-defined mountain valleys with a peak height of 11.1 nm. With the addition of 35 wt% salt, this height reduces to 9.6 nm. Surface roughness is crucial for enhancing ionic conductivity and is closely related to the material's amorphous nature. The salt addition alters the surface properties significantly, indicating its critical role in this aspect. By reducing the crystalline nature of the polymer blend, salt creates a more uniform surface, facilitating ion conduction.[52] This response was observed in this polymer system. The reduction in the maximum roughness height could be attributed to the consolidation of smaller pores, which merge to form larger globular structures, as observed in the SEM analysis. The expected enhancement in RMS roughness is likely to boost the interface between the electrode and the polymer electrolyte.[53] We noticed a substantial change in the form of the electrolyte films when salt was added. The electrolyte films containing 35 wt% $NaPF_6$ exhibit optimized solvent retention and consequently display a relatively smoother morphology.[54] Nevertheless, an increase in the maximum roughness height (9.6–27.9 nm) was observed with a higher salt content (40 wt%). The abrupt increase in roughness height may stem from the blocking effects caused by salt aggregation.[55]

3.9. Thermal Studies

Figure 10 shows the DSC thermograms of the proposed system. The glass transition temperature (T_g) is commonly determined as the midpoint of the step transition observed in a DSC curve, where it is marked by a noticeable change in slope. In the SPE system, the crystal melting peak is no longer observable, and only a single T_g is evident. This T_g increases nonlinearly from 51 to 81 °C with increasing sodium salt concentration. In comparison to the pristine blend F0, the elevated T_g values suggest the formation of ion–dipole interactions, resulting in a molecularly complex network.[56] This "transient physical" effect, arising from ion-dipole complexation, collectively hinders the segmental relaxation of polymer chains within the SPE system.[57] This transient cross-linking was a consequence of the interaction between the polymer functional groups and Na^+ cations. The lack of crystal melting, in conjunction with the nonlinear rise in the single

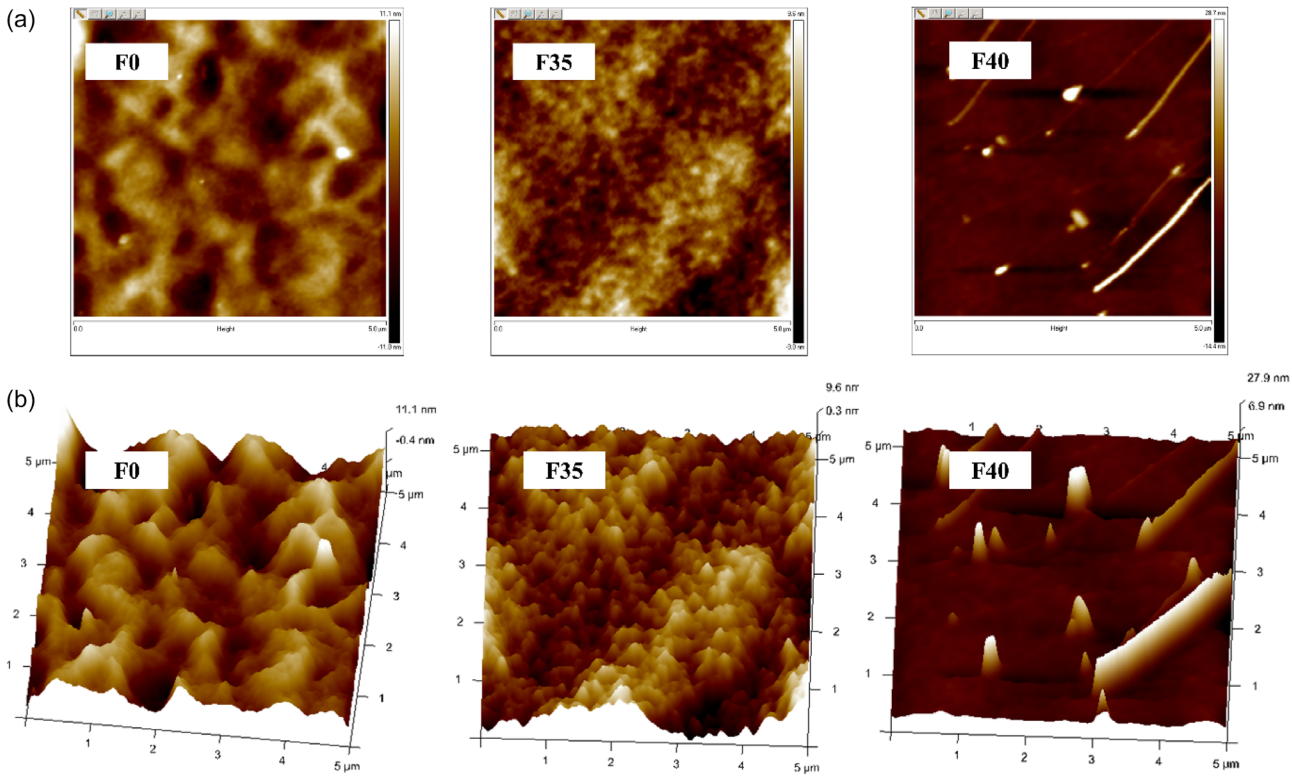

Figure 9. a) 2D and b) 3D AFM images of selected SPE samples.

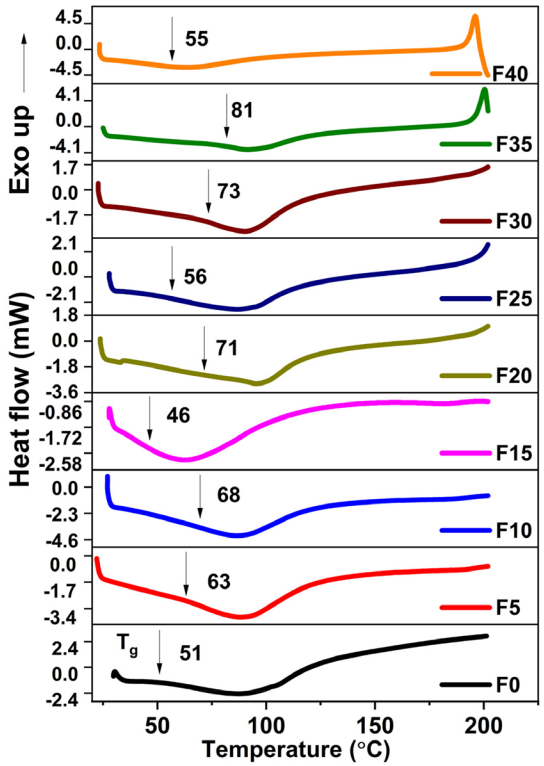

Figure 10. DSC thermograms of NaCMC/PVA-$NaPF_6$ SPEs.

T_g, suggests that the NaCMC/PVA SPEs possess an amorphous composition. The presence of exothermic peaks for F35 and F40 suggests that these polymer systems underwent significant decomposition (see TGA section).

Ensuring the safe operation of energy devices requires thorough thermal stability assessment prior to utilization. Decreased thermal stability can lead to electrolyte degradation, impacting ionic conductivity and overall performance in energy storage devices. Figure S3, Supporting Information, shows the thermogravimetric (TG) and derivative thermogravimetric (DTG) curves of the blend polymer with and without salt from room temperature to 500 °C. The graphs display three stages of mass loss. In the initial stage, a slight weight loss of ≈20% was observed between 27–250 °C, attributed to moisture loss absorbed during sample handling for TGA analysis.[58] The rate of weight loss was substantial (about 45%) between 250 and 300 °C, which could be ascribed to the process of decarboxylation. The third phase took place between ≈300 and 400 °C, resulting from the decomposition of residual carbon residues. Given the multiple peak temperatures displayed by the first derivative curve (DTG), we have determined the extrapolated onset temperature to be the maximum decomposition temperature, denoted as T_d. The temperature at which the major degradation step occurs for the F35 sample was found to be lower (190 °C) compared to the pure blend (240 °C), indicating a decline in thermal stability for the optimally conducting sample. This reduction in stability is believed to be caused

by the weakening of glycosidic bonds. The maximum temperature at which commercial EDLCs can operate is 80 °C. In contrast, our optimal conducting electrolyte remains stable at temperatures up to 190 °C.

3.10. Linear Sweep Voltammetry

ESW defines the secure operating limit for electrolytes in energy storage devices and is typically assessed using LSV in a sodiuml electrolytelinert planar electrode cell configuration, such as Pt or stainless steel (SS). Inert working electrodes are employed to avoid unwanted reactions and background current interference.[42] In this study, the working electrode's current was monitored as the potential increased linearly over time. Sodium amalgam (Na–Hg) was used as both the reference and counter electrode, with SS as the working electrode. The goal was to identify the potential at which SPE oxidizes or reduces, leading to degradation. The study determined an ESW of 3.56 V (**Figure 11**), a highly practical working potential for sodium-based energy storage devices.

3.11. Transference Number Measurements

Using Wagner's DC polarization method,[22] the transport number of ions was determined for the current blend SPE. Figure S4, Supporting Information, illustrates the correlation between polarization current and time. At the beginning, the observed higher current represents the total current, which includes both ionic and electronic elements. However, as time progresses, a steady state is achieved, which corresponds to the electronic current.[59] The SS electrodes function as a barrier, preventing the movement of ions through the external circuit, thereby permitting only the flow of electronic current.[59] The ion transport number and ionic conductivity were obtained by Equation (6) and (7) and is tabulated in **Table 6**.

The high ion transport number, near unity, and high ionic conductivity confirmed the predominantly ionic nature of the polymer films.[60]

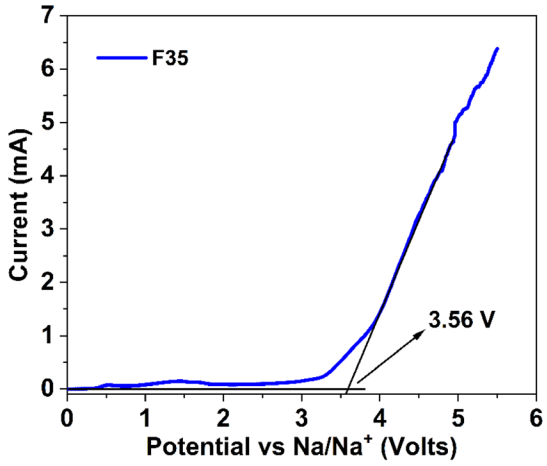

Figure 11. LSV graph for F35 sample.

Table 6. Variation of t_{ion} and ionic conductivity (σ_{ionic}) for NaCMC/PVA-$NaPF_6$ SPEs.

Sample	t_{ion}	σ_{ionic} [S cm^{-1}]
F5	0.97	9.16×10^{-07}
F10	0.99	1.68×10^{-06}
F15	0.98	2.72×10^{-06}
F20	0.99	3.87×10^{-06}
F25	0.99	9.41×10^{-06}
F30	0.99	1.32×10^{-05}
F35	0.99	2.21×10^{-05}
F40	0.99	1.93×10^{-05}

3.12. Mechanical Properties

Mechanical stability is essential when introducing energy storage devices, such as batteries, to the market. The polymer electrolyte must exhibit high ionic conductivity and transference number, along with suitable mechanical properties for long-term cycling stability. This stability is critical as the polymer electrolyte, situated between two electrodes during cell assembly, must endure applied pressure. Insufficient mechanical strength can lead to electrode short-circuiting. Thus, the material should be flexible to prevent brittleness and capable of absorbing minor shocks without impacting the electrodes. Mechanical strength also directly affects dendrite suppression/resistance, thereby enhancing safety.

Increasing the salt content in polymer electrolytes can improve ionic conductivity by providing more free ions for the charge transport. However, this can also negatively impact the polymer matrix, leading to a decrease in mechanical properties such as Young's modulus and tensile strength. Added salt causes plasticization of the polymer chains, which reduces their rigidity and consequently lowers the material's mechanical integrity. The stress and strain behaviors of the prepared polymer matrices, which are promising polymer electrolytes, were examined using an electromechanical testing machine. The stress–strain plots are shown in **Figure 12**. Stress–strain analysis indicated a deterioration in the mechanical strength of the polymer electrolyte system with the addition of $NaPF_6$. The NaCMC-PVA blend's mechanical properties transition from hard and brittle to soft and tough, depending on the percentage of salt incorporated. For the same amount of strain, the polymer electrolyte with a lower salt content can withstand a higher amount of stress than the electrolyte with a higher salt content.[61] Table S1, Supporting Information, demonstrates the changes in Young's modulus, tensile strength, and elongation at peak values for the NaCMC-PVA blend as the salt content varies.

As the salt content increased, both Young's modulus and tensile strength were observed to decrease. Conversely, the elongation at peak values was found to increase with higher salt content. The diminished mechanical strength of the blend in the presence of salt may be attributed to the way sodium ions interact with the polymer matrix, which primarily occurs intramolecularly rather than intermolecularly.[62] These findings

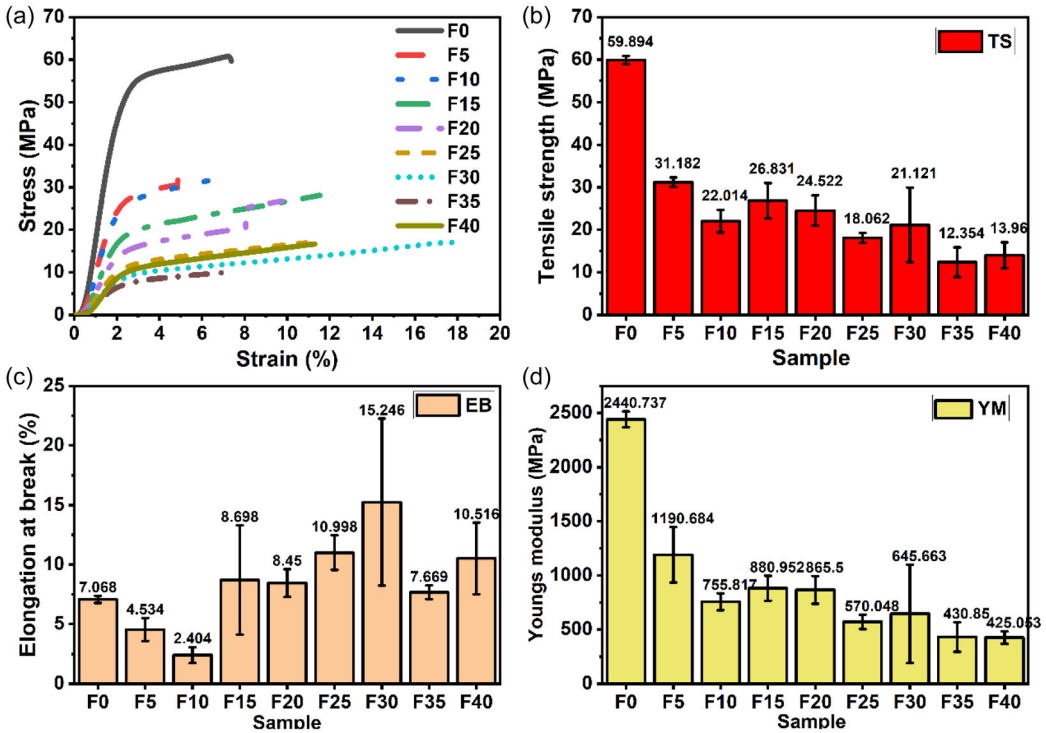

Figure 12. a) Stress–strain graph and b–d) variation of the mechanical parameters for NaCMC/PVA-$NaPF_6$ SPE.

suggest that the NaCMC-PVA blend becomes more amorphous with the addition of salt up to 35 wt% of salt.

3.13. Electrochemical Characterization of EDLC

3.13.1. Cyclic Voltammetry

CV is a common technique for assessing capacitive behavior and provides insights into the charge storage mechanism at the electrode–electrolyte interfaces distinguishing between non-Faradaic and Faradaic reactions. To determine the optimal working voltage window for the EDLC device, CV measurements were conducted at a scan rate of 5 mV s^{-1} (**Figure 13**a). It is well established that increasing the cell voltage significantly enhances the energy density of supercapacitors.[63] CV curves appear symmetric in the voltage window from 0 to 1 V, hence an operating voltage of 1 V was selected to balance performance and stability of the device.

After finding the suitable voltage window of 0–1 V, the performance of the EDLC employing F35 electrolyte was analyzed by CV at various scan rates at room temperature. Figure 13b illustrates the CV of the EDLC, transitioning from a leaf-like shape to nearly rectangular as the scan rate decreases from 100 to 5 mV s^{-1}. The deviation of the cyclic voltammogram from a perfect rectangular shape at higher scan rates can be attributed to internal resistance and porosity of the electrode material, resulting in a current–voltage dependence. As the scan rate decreases, a nearly rectangular shape without redox peaks is observed, indicating that capacitance is primarily stored by ion accumulation between the electrode–electrolyte interfaces, known as double-layer capacitance.[44]

Values of specific capacitance (C_s) at different scan rates were calculated using Equation (8) and are listed in **Table 7**. The decrease in C_s with increasing scan rate is attributed to increased energy loss and reduced stored charge on the electrode surface. At lower scan rates, ions have sufficient time to diffuse into vacant sites within the active electrode material, leading to a higher C_s value.[13]

CV can also be used to assess the stability and performance of an electrochemical cell over time, including evaluating the long-term stability of an EDLC after 3000 cycles, as shown in Figure 13c. CV analysis was performed after the device completed 3000 cycles, with the results indicating minimal change in specific capacitance, as seen in Table 7. This suggests that the EDLC maintains good electrochemical stability even after extensive cycling.

3.13.2. Charge–Discharge Analysis

In Figure 13d, the galvanostatic charge–discharge (GCD) profiles are presented at different applied currents within the potential range of 0–1 V, along with their corresponding calculated specific capacitance values tabulated in **Table 8**. The charge–discharge profiles exhibit a nearly triangular shape, indicating the non-Faradaic charge storage, consistent with the CV analysis, and indicate the absence of pseudo-capacitive effects such as ion adsorption and desorption. The specific capacitance (C_s) of the EDLC was calculated from the charge–discharge curves using Equation (9) and (10).

The energy density (E_d) and power density (P_d) were calculated using Equation (11) and (12,27) respectively. These parameters

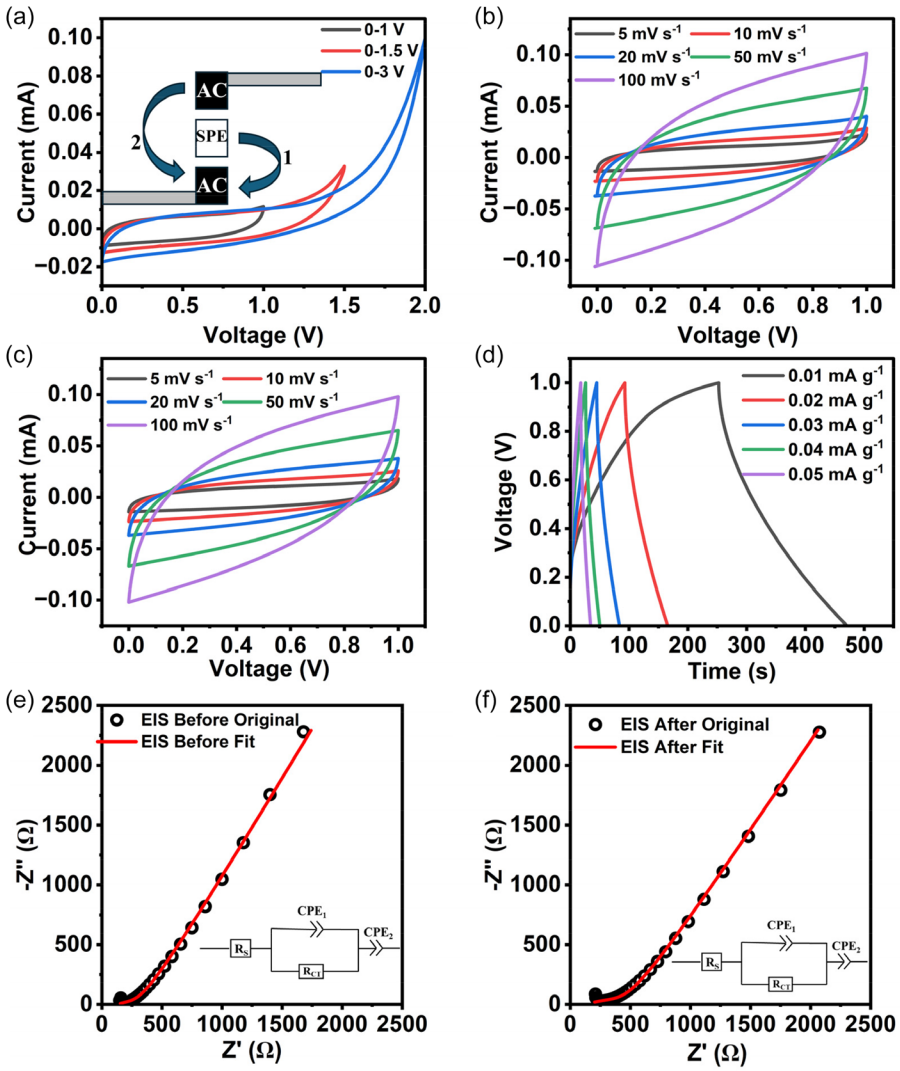

Figure 13. a) Cyclic voltammetry of EDLC device at different potential window (inset: schematic diagram of EDLC device), b) cyclic voltammetry of EDLC device (before cycling) at different scan rates, c) cyclic voltammetry of EDLC device (after cycling) at different scan rates, d) GCD of EDLC at different current densities, e) Nyquist plot of EDLC before cycling and f) Nyquist plot of EDLC after cycling.

Table 7. Specific capacitance using CV analysis at different scan rates.

Scan rate [mV s^{-1}]	Specific capacitance C_s [F g^{-1}] (before 3000 cycles)	Specific capacitance C_s [F g^{-1}] (after 3000 cycles)
100	2.02	1.9
50	2.76	2.64
20	4.1	3.9
10	5.2	5.2
5	6.4	6.4

Table 8. Specific capacitance, energy, and power density calculated using GCD at different current density.

Current density [mA g^{-1}]	Specific capacitance [F g^{-1}]	Energy density [W kg^{-1}]	Power density [Wh kg^{-1}]
0.1	9.53	0.979	43
0.2	2.28	0.178	75
0.3	1.26	0.076	99
0.4	0.83	0.045	126
0.5	0.42	0.022	155

are crucial for evaluating the performance of an EDLC. Energy density represents the amount of energy a device can store per unit mass, while power density measures the rate at which this energy can be delivered per unit mass. Table 8 presents the calculated E_d and P_d values of the EDLC at various current densities in this study. The polymer electrolyte plays a dual role within the EDLC, acting as both an ion supplier for the positive (+) and negative (−) electrodes and as an ion conductor. This multifunctionality has a significant impact on the device's performance.

3.13.3. EIS Measurements

The electrochemical reaction process is further explored using electrochemical impedance spectroscopy (EIS) technique.[64] By applying an amplitude of 5 mV over a frequency range of 1 MHz to 0.01 Hz, EIS provides insights into the electrochemical behavior of the EDLC. Figure 13e illustrates Nyquist plots of the EDLC device with F35 SPE. The low-frequency regions of the Nyquist plot exhibit a spike and small semicircle at high-frequency region represents charge transfer resistance (R_{ct}). Utilizing EC-lab software, the Nyquist plot is fitted with an equivalent circuit as shown in inset of Figure 13e. It is evident that the equivalent circuit comprises an ohmic serial resistance (R_s) in conjunction with a parallel combination of charge transfer resistance (R_{ct}) and a constant phase element (CPE1). Additionally, there is a series with another constant phase element (CPE2). Equivalent series resistance (ESR) (R_s), which results from internal resistance, resistance of connecting wire and its connections, is the first Nyquist plot intersection with the real axis at low frequencies. The charge transfer resistance between the electrode and the electrolyte is the cause of the second Nyquist plot (R_{ct}) intersection with the real axis. The device's capacitive behavior because of charge adsorption and intercalation causes the inclined line to appear in the high frequency area. Spike formation in the F35 SPE EDLC indicates significant charge accumulation at the electrode–electrolyte interface, which is caused by the presence of ions.[65]

Table 9. Estimated parameters of the equivalent circuit elements in model used for fitting Nyquist plot before and after cycling.

Element	Cycling state	Values
R_s [Ω]	Before	124
	After	120
R_{ct} [Ω]	Before	406
	After	605
CPE1 [$Fcm^{-2}\,s^{(n_1^{-1})}$]	Before	1.206×10^{-3}
	After	0.577×10^{-3}
CPE2 [$Fcm^{-2}\,s^{(n_2^{-1})}$]	Before	0.517×10^{-3}
	After	0.495×10^{-3}

The internal resistance (R_s) values of the EDLC device before cycling test were found to be, 124 Ω indicating good ionic conductivity. The charge transfer resistance (R_{ct}) was found to be 406 Ω, suggesting comparable reaction kinetics and excellent chemical stability of the electrolyte materials. The results presented in **Table 9** obtained by Nyquist plot after cycling (Figure 13f) suggested no potential degradation occurred during long-term cycling, and the material retained its original properties as supported by CV analysis performed after cycling test.

3.13.4. Capacity Retention, Efficiency and ESR over Cycling

The cyclic performance of EDLC devices is a significant indication for its real applications. A prolonged cycle life with consistent capacitance is considered a crucial criterion for an EDLC. The device was tested for its cycling stability for 3000 cycles at 0.2 mA g^{-1} current density, and it was observed that capacitance decreased slightly by the end of 3000 cycles as shown in **Figure 14**a. During the cycling of an EDLC, gradual decrease

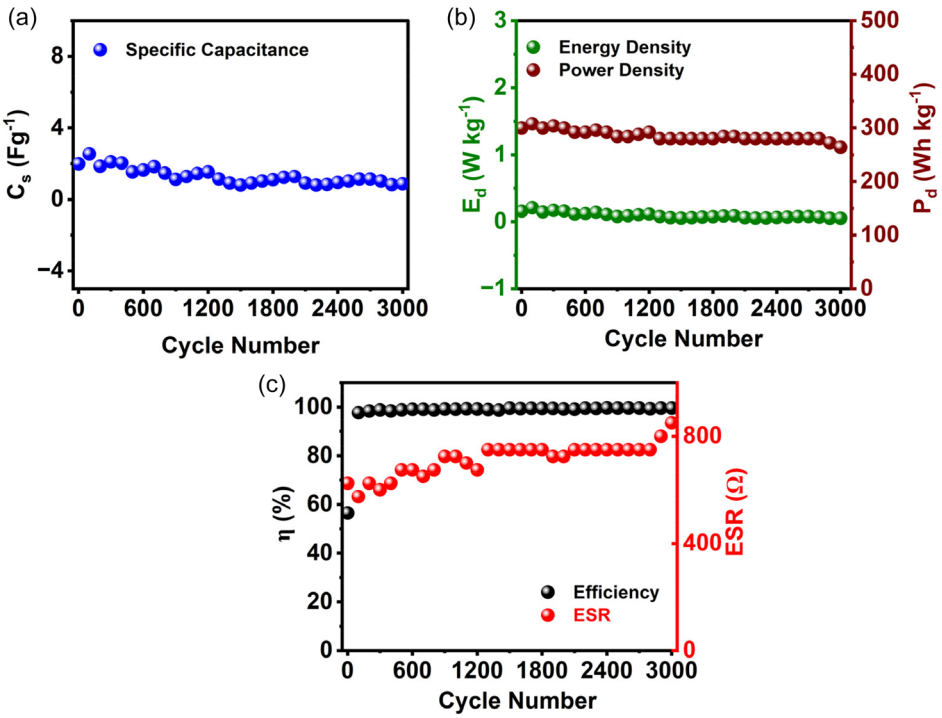

Figure 14. a) Specific capacitance of the EDLC cell after performing cycling test for 3000 cycles, b) energy density and power density for 3000 cycles, and c) efficiency and ESR for 3000 cycles at current density of 0.2 mA g^{-1}.

in capacitance may be attributed to electrode surface degradation, electrolyte decomposition, pore structure alterations, and the formation of unwanted surface films. These factors collectively reduce the available surface area for charge storage within the electric double layer, leading to a decrease in capacitance.

Another important metric for assessing the cycle stability of an EDLC is the coulombic efficiency (η), which can be calculated (equation 27) using the following formula

$$\eta = \frac{t_d}{t_c} \times 100\% \tag{27}$$

where t_d and t_c represent the discharge and charge times, respectively. Figure 14c shows the columbic efficiency (η) of the EDLC over 3000 cycles at low current density of 0.2 mA g^{-1}. The columbic efficiency of the EDLC remained steady at 98–99% throughout 3000 cycles. This high and consistent efficiency throughout the cycling test suggests good long-term stability of the EDLC in this work. It also signifies stable and reliable electrode–electrolyte contact during cycling.[66]

Another key desirable feature of an EDLC assembly is low ESR.[67] ESR is influenced by four main factors: the intrinsic resistance of the active electrode material, the bulk resistance within the electrolyte, the current collector, and the contact resistance between the active material and electrolyte.[68] The ESR was calculated utilizing the cycling data using the equation 28

$$\mathrm{ESR} = \frac{iR_{\mathrm{drop}}}{2I} \tag{28}$$

An insight into the EDLC assembly can be obtained from the ESR response over multiple cycles, as illustrated in Figure 14c. The ESR value is recorded at 600 Ω in the first cycle and remains relatively stable around 750 Ω. This high ESR is primarily attributed to electrolyte resistance, which is influenced by the electrolyte's conductivity. Electrolyte resistance reflects the ion transport resistance within the porous electrode material, across the electrode layer, and through the bulk electrolyte solution. In this study, the high value of ESR may be linked to the electrolyte's lower ionic conductivity which was in the order of 10^{-5} S cm^{-1}. A comparison of the EDLC parameters from this study with previously reported systems is presented in **Table 10**.

The incorporation of plasticizers or ionic liquids will be explored in future work to further reduce ESR and enhance electrolyte conductivity.

Table 10. Parameters of the fabricated EDLC in this report compared with previously reported systems.

Electrolyte system	Specific capacitance	Energy density [Wh kg^{-1}]	Power density [W kg^{-1}]	Reference
NaCMC-PVA-$NaClO_4$	18.4 Fg^{-1}@5 mV s^{-1}	15.18	4512.5	[18]
CMC-PVA-$LiClO_4$	97.25 Fg^{-1}@2 mV s^{-1}	3.16	402.95	[13]
Dextran-NH_4Br	2.46 Fg^{-1}@50 mV s^{-1}	–	–	[69]
Chitosan-PEO-$LiClO_4$	6.88 Fg^{-1}@0.5 mA cm^{-2}	1.07	321	[70]
NaCMC-PVA-$NaPF_6$	6.4 Fg^{-1}@5 mV s^{-1}	0.979	43	Present work

4. Conclusion

This study successfully demonstrated a new biopolymer electrolyte using NaCMC/PVA and $NaPF_6$ salts for EDLC applications. The SPE shows an ionic conductivity enhancement from 10^{-7} to 10^{-5} S cm^{-1} with salt doping up to 35 wt%. This was predominantly due to the availability of more free ions provided by the $NaPF_6$ salt. However, beyond this concentration, the conductivity starts to decrease because the formation of larger ion pairs/clusters hinders ionic motion. TNM verify that the system is primarily ionic in nature, while the stability window of the SPEs is demonstrated to be favorable through LSV analysis. Doping salt into a biopolymer blend matrix not only enhances conductivity but also reduces the crystallinity of biopolymer electrolytes, as confirmed by XRD analysis. The optimized SPE film (F35) exhibits a significant electrochemical stability of 3.56 V and sufficient tensile strength of 12.354 ± 3.507 MPa, which is suitable for electrochemical device applications, including EDLCs. The CV plot obtained for the EDLC displays a nearly rectangular shape at lower scan rates, which confirms the capacitive behavior of the EDLC. The EDLC's characteristics are further analyzed through GCD measurements. The device demonstrated a specific capacitance of 9.53 F g^{-1}, an energy density of 0.979 W kg^{-1}, and a power density of 43 Wh kg^{-1} at a current of 0.1 mA g^{-1}. In addition, the device was tested for its cycling stability over 3000 cycles, and it was observed that the device maintained its capacitance consistently until the end of 3000 cycles. While the existing conductivity level meets the requirements for some applications, advancing it could substantially boost device performance. Integrating plasticizers or ionic liquids offers a promising route to achieve this enhancement by increasing ionic mobility within the polymer matrix. Such improvements would facilitate better electrode–electrolyte contact, reduce internal resistance, and enhance charge/discharge efficiency. Therefore, further exploration of these modifications is recommended to optimize materials for supercapacitor applications, potentially leading to devices with superior energy and power densities.

Supporting Information

Supporting Information is available from the Wiley Online Library or from the author.

Acknowledgements

One of the authors, V.C., extends his gratitude to the Directorate of Minorities in Bengaluru, India, for their support. V.C. is particularly thankful for the financial assistance provided in the form of a fellowship for minority students, as per the sanction order DOM/Fellowship/CR-10/2019-20 dated June 29, 2020, which made this research possible.

Conflict of Interest

The authors declare no conflict of interest.

Author Contributions

Vipin Cyriac: conceptualization; data curation (lead); formal analysis (lead); investigation (lead); methodology (lead); writing–original draft (lead). **Ismayil**: methodology (equal); resources (lead); supervision (lead); validation (lead); writing–review & editing (equal). **Kuldeep Mishra**: resources (supporting); validation (supporting). **Ankitha Rao**: investigation (supporting); formal analysis (supporting). **Saraswati P. Masti**: formal analysis (supporting); resources (supporting); validation (supporting). **I. M. Noor**: validation (supporting); formal analysis (supporting); writing–review & editing (equal).

Data Availability Statement

The data that support the findings of this study are available from the corresponding author upon reasonable request.

Keywords

dielectric properties, electric double-layer capacitors, ionic conductivity, Nyquist plot, polymer electrolytes

Received: March 8, 2025
Revised: April 13, 2025
Published online: June 6, 2025

[1] P. Vashishta, J. N. Mundy, G. K. Shenoy, *Proc. of the International Conf. on Fast Ion Transport in Solids, Electrodes, and Electrolytes*, Lake Geneva, Wisconsin, U.S.A., May 21–25 **1979**, *744*.
[2] J. B. Goodenough, *Proc. R. Soc. Lond. A. Math. Phys. Sci.* **1984**, *393*, 215.
[3] D. E. Fenton, J. M. Parker, P. V. Wright, *Polymer* **1973**, *14*, 589.
[4] S. B. Aziz, T. J. Woo, M. F. Z. Kadir, H. M. Ahmed, *J. Sci. Adv. Mater. Dev.* **2018**, *3*, 1.
[5] R. Chen, W. Qu, X. Guo, L. Li, F. Wu, *Mater. Horiz.* **2016**, *3*, 487.
[6] J. W. Fergus, *J. Power Sources* **2010**, *195*, 4554.
[7] R. T. Abdulwahid, S. B. Aziz, M. F. Z. Kadir, *Mater. Today Sustainability* **2023**, *23*, 100472.
[8] N. F. Mazuki, N. M. J. Rasali, M. A. Saadiah, A. S. Samsudin, *AIP Conf. Proc.* **2018**, 2030.
[9] S. El-Gamal, A. M. El Sayed, E. E. Abdel-Hady, *J. Polym. Environ.* **2018**, *26*, 2536.
[10] A. M. Shehap, *Egyptian J. Solids* **2008**, *31*, 75.
[11] V. Tyagi, A. Thakur, *Mater. Today Proc.* **2023**, https://doi.org/10.1016/j.matpr.2023.01.042.
[12] N. F. Mazuki, A. F. Fuzlin, M. A. Saadiah, A. S. Samsudin, *Ionics* **2019**, *25*, 2657.
[13] A. Zulkifli, M. A. Saadiah, N. F. Mazuki, A. S. Samsudin, *Mater. Chem. Phys.* **2020**, *253*, 123312.
[14] M. A. Saadiah, Y. Nagao, A. S. Samsudin, *Int. J. Hydrogen Energy* **2020**, *45*, 14880.
[15] N. S. Mohd Ali, Y. Nagao, A. S. Samsudin, *Makara J. Technol.* **2020**, *24*, 1.
[16] V. Cyriac, Ismayil, I. M. Noor, K. Mishra, C. Chavan, R. F. Bhajantri, S. P. Masti, *Cellulose* **2022**, *29*, 3271.
[17] V. Cyriac, Ismayil, I. S. B. M. Noor, Z. E. Rojudi, Y. N. Sudhakar, C. Chavan, R. F. Bhajantri, M. S. Murari, *Int. J. Energy Res.* **2022**, *46*, 22845.
[18] V. Cyriac, Ismayil, K. Mishra, A. Rao, S. P. Masti, I. M. Noor, *Electrochim. Acta* **2024**, *507*, 145139.
[19] Q. Zhang, Y. Lu, H. Yu, G. Yang, Q. Liu, Z. Wang, L. Chen, Y.-S. Hu, *J. Electrochem. Soc.* **2020**, *167*, 070523.
[20] O. V. Lonchakova, O. A. Semenikhin, M. V. Zakharkin, E. A. Karpushkin, V. G. Sergeyev, E. V. Antipov, *Electrochim. Acta* **2020**, *334*, 135512.
[21] M. A. Saadiah, D. Zhang, Y. Nagao, S. K. Muzakir, A. S. Samsudin, *J. Non Cryst. Solids* **2019**, *511*, 201.
[22] J. B. Wagner, C. Wagner, *J. Chem. Phys.* **1957**, *26*, 1597.
[23] B. Andres, A. C. Engström, N. Blomquist, S. Forsberg, C. Dahlström, H. Olin, *PLoS One* **2016**, *11*, e0163146.
[24] A. Iakunkov, V. Skrypnychuk, A. Nordenström, E. A. Shilayeva, M. Korobov, M. Prodana, M. Enachescu, S. H. Larsson, A. Vtalyzin, *Phys. Chem. Chem. Phys.* **2019**, *21*, 17901.
[25] M. D. Stoller, R. S. Ruoff, *Energy Environ. Sci.* **2010**, *3*, 1294.
[26] D. Sun, X. Yan, J. Lang, Q. Xue, *J. Power Sources* **2013**, *222*, 52.
[27] S. T. Senthilkumar, R. K. Selvan, Y. S. Lee, J. S. Melo, *J. Mater. Chem. A Mater.* **2012**, *1*, 1086.
[28] P. M. Pandian, A. Pandurangan, *Diam. Relat. Mater.* **2021**, *118*, 108495.
[29] T. Qin, S. Peng, J. Hao, Y. Wen, Z. Wang, X. Wang, D. He, J. Zhang, J. Hou, G. Cao, *Adv. Energy Mater.* **2017**, *7*, 1700409.
[30] V. Cyriac, S. Molakalu Padre, Ismayil, G. Sangam Chandrashekar, C. Chavan, R. Fakeerappa Bhajantri, M. S. Murari, *J. Appl. Polym. Sci.* **2022**, *139*, e52525.
[31] A. Arya, A. L. Sharma, *J. Phys.: Condens. Matter* **2018**, *30*, 165402.
[32] C. Chavan, R. F. Bhajantri, V. Cyriac, Ismayil, S. S. Bulla, K. Sakthipandi, *Polym. Adv. Technol.* **2023**.
[33] F. Menges, Spectragryph - Optical Spectroscopy Software, Version 1.2. 14. Oberstdorf, Germany, Available online: https://www.effemm2.de/spectragryph **2019**.
[34] C. Bhatt, R. Swaroop, A. Arya, A. L. Sharma, *J. Mater. Sci. Eng. B* **2015**, *5*, 418.
[35] Pritam, A. Arya, A. L. Sharma, *Ionics* **2020**, *26*, 745.
[36] J. L. Tyler, R. L. Sacci, J. Nanda, *Energies* **2021**, *14*, 4409.
[37] M. F. Shukur, M. F. Z. Kadir, *Electrochim. Acta* **2015**, *158*, 152.
[38] H. Dai, Y. Huang, H. Huang, *Carbohydr. Polym.* **2018**, *185*, 1.
[39] M. P. Aji, Masturi, S. Bijaksana, Khairurrijal, M. Abdullah, *Am. J. Appl. Sci.* **2012**, *9*, 946.
[40] R. M. Hodge, G. H. Edward, G. P. Simon, *Polymer* **1996**, *37*, 1371.
[41] A. Galeski, A. S. Argon, R. E. Cohen, *Macromolecules* **1991**, *24*, 3945.
[42] V. Cyriac, Ismayil, K. Mishra, Y. N. Sudhakar, Z. E. Rojudi, S. P. Masti, I. M. Noor, *Solid State Ion.* **2024**, *411*, 116578.
[43] A. S. Marf, R. M. Abdullah, S. B. Aziz, *Membranes* **2020**, 10.
[44] M. F. Shukur, R. Ithnin, M. F. Z. Kadir, *Electrochim. Acta* **2014**, *136*, 204.
[45] A. K. Arof, S. Amirudin, S. Z. Yusof, I. M. Noor, *Phys. Chem. Chem. Phys.* **2014**, *16*, 1856.
[46] B. M. Greenhoe, M. K. Hassan, J. S. Wiggins, K. A. Mauritz, *J. Polym. Sci. B Polym. Phys.* **2016**, *54*, 1918.
[47] K. A. Mauritz, *Macromolecules* **1989**, *22*, 4483.
[48] A. Arya, A. L. Sharma, **2018**, *29*, 17903.
[49] R. K. Prajapati, H. Kumar, A. L. Saroj, *Phys. B Condens. Matter* **2023**, *662*, 414962.
[50] S. B. Aziz, S. Al-Zangana, H. J. Woo, M. F. Z. Kadir, O. G. Abdullah, *Results Phys.* **2018**, *11*, 826.
[51] P. Ding, Z. Lin, X. Guo, L. Wu, Y. Wang, H. Guo, L. Li, H. Yu, *Mater. Today* **2021**, *51*, 449.
[52] A. Arya, A. L. Sharma, *J. Solid State Electrochem.* **2018**, *22*, 2725.
[53] K. M. Manikandan, A. Yelilarasi, P. Senthamaraikannan, S. S. Saravanakumar, A. Khan, A. M. Asiri, *J. Solid State Electrochem.* **2018**, *22*, 3785.
[54] C. Maheshwaran, D. K. Kanchan, K. Mishra, D. Kumar, K. Gohel, *Nano-Struct. Nano-Objects* **2020**, *24*, 100587.

[55] V. Parthiban, S. Akula, S. G. Peera, N. Islam, A. K. Sahu, *Energy Fuels* **2016**, *30*, 725.
[56] R. He, T. Kyu, *Macromolecules* **2016**, *49*, 5637.
[57] N. A. Stolwijk, C. Heddier, M. Reschke, M. Wiencierz, J. Bokeloh, G. Wilde, *Macromolecules* **2013**, *46*, 8580.
[58] F. Colò, F. Bella, J. R. Nair, M. Destro, C. Gerbaldi, *Electrochim. Acta* **2015**, *174*, 185.
[59] R. A. Khellouf, S. Durpekova, V. Cyriac, J. Cisar, C. Bubulinca, A. Lengalova, D. Skoda, V. Sedlarík, *Solid State Ion.* **2023**, *402*, 116379.
[60] V. Cyriac, Ismayil, Y. N. Sudhakar, K. Mishra, Z. E. Rojudi, M. S. Murari, I. M. Noor, *Mater. Res. Bull.* **2024**, *169*, 112498.
[61] S. Ramesh, T. Winie, A. K. Arof, *Eur. Polym. J.* **2007**, *43*, 1963.
[62] M. M. E. Jacob, A. K. Arof, *Polym. Eng. Sci.* **2000**, *40*, 972.
[63] W. G. Nunes, B. G. A. Freitas, R. M. Beraldo, R. M. Filho, L. M. Da Silva, H. Zanin, *Sci. Rep.* **2020**, *10*, 19195.
[64] S. Shenbagavalli, M. Muthuvinayagam, M. S. Revathy, *J. Energy Storage* **2022**, *55*, 105726.
[65] N. Farah, H. M. Ng, A. Numan, C. W. Liew, N. A. A. Latip, K. Ramesh, S. Ramesh, *Mater. Sci. Eng. B* **2019**, *251*, 114468.
[66] S. Aziz, E. Dannoun, R. Abdulwahid, M. Kadir, M. Nofal, S. Al-Saeedi, A. Murad, *Membranes* **2022**, *12*, 139.
[67] H. D. Yoo, J. H. Jang, J. H. Ryu, Y. Park, S. M. Oh, *J. Power Sources* **2014**, *267*, 411.
[68] S. B. Aziz, M. H. Hamsan, M. M. Nofal, W. O. Karim, I. Brevik, M. A. Brza, R. T. Abdulwahid, S. Al-Zangana, M. F. Z. Kadir, *Polymers* **2020**, *12*, 1411.
[69] M. H. Hamsan, M. F. Shukur, S. B. Aziz, Y. M. Yusof, M. F. Z. Kadir, *Bull. Mater. Sci.* **2020**, *43*, 30.
[70] S. B. Aziz, M. H. Hamsan, M. A. Brza, M. F. Z. Kadir, R. T. Abdulwahid, H. O. Ghareeb, H. J. Woo, *Results Phys.* **2019**, *15*, 102584.